ARTICLE

https://doi.org/10.1038/s41586-019-1564-x

Glutamatergic synaptic input to glioma cells drives brain tumour progression

Varun Venkataramani[1,2,3]*, Dimitar Ivanov Tanev[1,2,3], Christopher Strahle[1], Alexander Studier-Fischer[2,3], Laura Fankhauser[2,3], Tobias Kessler[2,3], Christoph Körber[1], Markus Kardorff[1], Miriam Ratliff[3,4], Ruifan Xie[2,3], Heinz Horstmann[1], Mirko Messer[2,3], Sang Peter Paik[1], Johannes Knabbe[1], Felix Sahm[5,6], Felix T. Kurz[7], Azer Aylin Acikgöz[8], Frank Herrmannsdörfer[1], Amit Agarwal[9,10], Dwight E. Bergles[10], Anthony Chalmers[11], Hrvoje Miletic[12,13], Sevin Turcan[2], Christian Mawrin[14], Daniel Hänggi[4], Hai-Kun Liu[8], Wolfgang Wick[2,3], Frank Winkler[2,3,15]* & Thomas Kuner[1,15]*

A network of communicating tumour cells that is connected by tumour microtubes mediates the progression of incurable gliomas. Moreover, neuronal activity can foster malignant behaviour of glioma cells by non-synaptic paracrine and autocrine mechanisms. Here we report a direct communication channel between neurons and glioma cells in different disease models and human tumours: functional bona fide chemical synapses between presynaptic neurons and postsynaptic glioma cells. These neurogliomal synapses show a typical synaptic ultrastructure, are located on tumour microtubes, and produce postsynaptic currents that are mediated by glutamate receptors of the AMPA subtype. Neuronal activity including epileptic conditions generates synchronised calcium transients in tumour–microtube–connected glioma networks. Glioma-cell-specific genetic perturbation of AMPA receptors reduces calcium-related invasiveness of tumour–microtube-positive tumour cells and glioma growth. Invasion and growth are also reduced by anaesthesia and the AMPA receptor antagonist perampanel, respectively. These findings reveal a biologically relevant direct synaptic communication between neurons and glioma cells with potential clinical implications.

The relationship between neuronal structures and glioma cells in humans is well described[1] and has been attributed to a paracrine growth-promoting mechanism involving the neuroligin-3 neuronal protein[2,3]. Nonsynaptic autocrine and paracrine effects of classical neurotransmitters have also been associated with progression of gliomas and other tumour entities. In particular, glutamate can enhance the proliferation, survival and invasiveness of tumour cells after binding to different classes of glutamate receptors[4–9]. Furthermore, the progression and resistance of incurable gliomas, particularly glioblastomas (GBs) and lower grade astrocytic gliomas, are promoted by tumour microtubes (TMs)[10,11]. These are long, cellular processes of glioma cells driven by pathways involved in neurodevelopment and neuroplasticity[10,11]. TMs are crucial for the invasion and proliferation of glioma cells and connect single tumour cells to a functional communicating network[10,12]. Whether TMs are also involved in neuron–glioma interactions is unknown.

Ultrastructural identity of neurogliomal synapses

While using electron microscopy to examine TMs, we noticed contacts typical for chemical synapses (Fig. 1a–d, Extended Data Figs. 1–3). We probed for the existence of such neurogliomal synapses (NGS) in different model systems, including six patient-derived human GB cell lines (BG5, S24, T1, T269, T325 and E2) xenografted into mice (patient-derived xenograft (PDX) models, Supplementary Table 1) or co-cultured with neurons, a genetic mouse model[13], as well as resected human tumour material from ten adult patients with GB and isocitrate dehydrogenase (IDH)-mutant grade II and III astrocytoma according to WHO (World Health Organization) classification (Supplementary Table 2). Tumour cells and their TMs were unambiguously identified by several counterstaining methods (Extended Data Fig. 1, Supplementary Discussion 1.3). In all conditions we reproducibly and frequently found NGS in the tumour infiltration zone (Fig. 1, Extended Data Fig. 2, Supplementary Discussion 1.4). NGS typically contain a cluster of presynaptic vesicles, a synaptic cleft with electron-dense material, a presynaptic active zone matrix with docked vesicles, and a postsynaptic density area, showing all the hallmark features of a glutamatergic chemical synapse[14,15] (Fig. 1, Extended Data Figs. 1f, g, 2a–r, 3a–q, s, t, Supplementary Videos 1–4, Supplementary Discussion 1.5–6).

NGS uniformly consisted of a presynaptic neuronal and a postsynaptic gliomal part, with no evidence for synapses in the reverse direction or synapses between glioma cells in any human or mouse sample investigated ($n > 200$ NGS analysed; Fig. 1e, Extended Data Fig. 3r, Supplementary Table 3, Supplementary Discussion 1.7).

To characterize the structural repertoire of NGS further, 3D ultrastructural reconstructions from serial electron microscopy sections were generated (Extended Data Figs. 2l, m, q, r, 3a–q). Contacts between neurons and glioma cells occurred in three morphological categories, possibly contributing different functional properties (Fig. 1e, Extended Data Fig. 3a–c): (1) a single synaptic contact on a glioma TM; (2) a multisynaptic contact to both a glioma TM and a neuron; and (3) a TM approaching an existing neuronal synapse with contact to the synaptic cleft, but without showing ultrastructural details of a bona-fide synapse.

[1]Department of Functional Neuroanatomy, Institute for Anatomy and Cell Biology, Heidelberg University, Heidelberg, Germany. [2]Neurology Clinic and National Center for Tumor Diseases, University Hospital Heidelberg, Heidelberg, Germany. [3]Clinical Cooperation Unit Neurooncology, German Cancer Consortium (DKTK), German Cancer Research Center (DKFZ), Heidelberg, Germany. [4]Neurosurgery Clinic, University Hospital Mannheim, Mannheim, Germany. [5]Department of Neuropathology, Institute of Pathology, Ruprecht-Karls University Heidelberg, Heidelberg, Germany. [6]Clinical Cooperation Unit Neuropathology, German Cancer Consortium (DKTK), German Cancer Research Center (DKFZ), Heidelberg, Germany. [7]Department of Neuroradiology, University Hospital Heidelberg, Heidelberg, Germany. [8]Division of Molecular Neurogenetics, DKFZ-ZMBH Alliance, German Cancer Research Center (DKFZ), Heidelberg, Germany. [9]The Solomon H. Snyder Department of Neuroscience, Johns Hopkins University School of Medicine, Baltimore, MD, USA. [10]CHS Research Group, Institute for Anatomy and Cell Biology, Heidelberg University, Heidelberg, Germany. [11]Institute of Cancer Sciences, University of Glasgow, Glasgow, UK. [12]Department of Biomedicine, University of Bergen, Bergen, Norway. [13]Department of Pathology, Haukeland University Hospital, Bergen, Norway. [14]Institute for Neuropathology, Otto-von-Guericke University, Magdeburg, Germany. [15]These authors jointly supervised this work: Frank Winkler, Thomas Kuner. *e-mail: varun.venkataramani@med.uni-heidelberg.de; frank.winkler@med.uni-heidelberg.de; thomas.kuner@uni-heidelberg.de

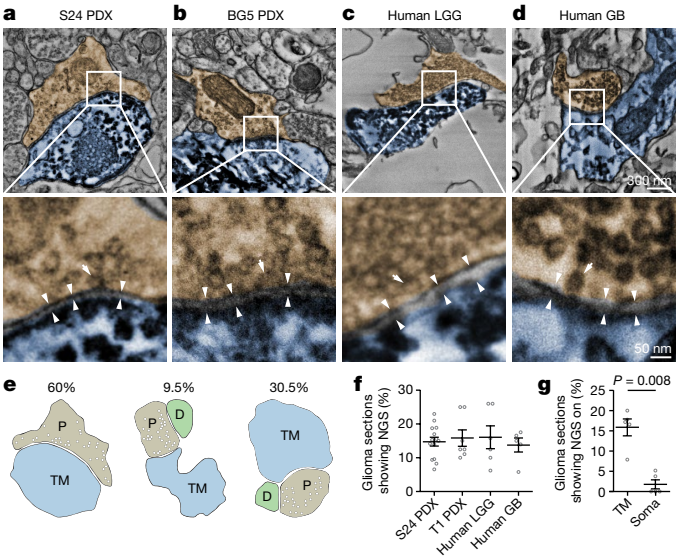

Fig. 1 | Ultrastructure of neuroglioma synapses in mouse models and patient tumours. a–d, Representative immuno-electron microscopy images of synapses between presynaptic axons (sepia) and postsynaptic glioma cell TMs (blue), in patient-derived GB xenografts (S24 and BG5 glioma cell lines) and in resected tissue of patients with glioma (see **f** for sample size). Electron-dense DAB (3,3′-diaminobenzidine) precipitate marks glioma cells (see Extended Data Fig. 1, Supplementary Information). Arrowheads denote synaptic clefts; arrows denote docked vesicles. LGG, low-grade glioma. **e**, Morphological classification of NGS (see text, Extended Data Fig. 3a–c). D, dendrite; P, presynapse. **f**, Percentage of randomly selected electron microscopy sections showing NGS (14 tissue blocks from S24 PDX from 5 mice; 7 tissue blocks from T1 PDX from 3 mice; 5 blocks from BG5 PDX from 1 mouse; 6 tissue blocks from 2 human patients with LGG; 5 tissue blocks from 3 human patients with GB). **g**, Localization of NGS on TMs versus somata of S24 PDX glioma cells ($n = 313$ glioma TM sections and $n = 44$ glioma cell soma sections analysed from 5 S24 PDX mice). *P* value determined by two-sided Mann–Whitney test. Data are mean ± s.e.m.

NGS were detectable on 13.8–16.0% of tumour sections from different mouse models and patient gliomas (Fig. 1f). Most NGS could be found on TMs of glioma cells (Fig. 1g). In an oligodendroglioma and meningioma model—two primary brain tumour types that can be curable and that grow without relevant TM formation—synapses between neurons and tumour cells were not detectable (Extended Data Fig. 2u–x).

In conclusion, NGS are consistently formed in incurable human gliomas and mouse models thereof, but not in less malignant primary brain tumours, suggesting a specific contribution to the malignant features of astrocytic gliomas, including GB.

Molecular composition of NGS

To support a glutamatergic identity of NGS (Fig. 2), we first used super-resolution 3D direct stochastic optical reconstruction microscopy (*d*STORM) to unequivocally identify the postsynaptic density markers HOMER1, HOMER2 and HOMER3 within a TM and to reveal the corresponding glutamatergic synaptic vesicle cluster (identified by labelling of VGLUT1) (Fig. 2a). Furthermore, using confocal microscopy, we identified glutamatergic AMPA (α-amino-3-hydroxy-5-methyl-4-isoxazole propionic acid) receptors in NGS organized in a strictly punctate pattern and overlapping with glutamatergic presynaptic vesicle clusters (Extended Data Fig. 4a). Of note, across xenograft models and resected human GB material, more than 80% of AMPA receptor (AMPAR) signals on TMs colocalized with a presynaptic signal, which demonstrates synaptic rather than extrasynaptic expression of AMPAR by GB cells (Extended Data Fig. 4b). To examine the repertoire of synaptic proteins expressed by brain tumour cells, we analysed single-cell gene expression data of human gliomas[16,17]. We found that AMPARs were most robustly expressed in a fraction of GB and IDH-mutated astrocytoma single cells (Fig. 2d, Extended Data Fig. 4c, d). Consistent with a previous study[18], *GRIA2* mRNA—which encodes the GluA2 subunit of AMPARs—was incompletely edited in human IDH-mutated gliomas, predicting the expression of Ca^{2+} permeable AMPAR[19,20] in glioma cells (Extended Data Fig. 4e, f). Incomplete editing was particularly pronounced in the prognostically unfavourable astrocytomas compared with 1p/19q co-deleted oligodendrogliomas, and in the known GB gene expression subgroups (proneural, classical and mesenchymal). Furthermore, most tumour cells expressed at least one of the five genes that are most prominently involved in synaptogenesis[21] (Extended Data Fig. 4g, h), consistent with a reported glioma cell subpopulation with synaptogenic properties during tumour progression[22]. 3D electron microscopy and immunofluorescence staining further revealed that glutamatergic NGS are frequently expressed on interconnected TM networks[10] (Fig. 2b, c, Extended Data Fig. 4i–k). To gain further insight into the TM-positive GB cell subpopulation that expresses AMPAR subunits, we discriminated TM-connected versus TM-unconnected GB cells based on their differential uptake of the SR101 fluorescent dye (Fig. 2e, Extended Data Fig. 4l, Supplementary Information 1.8), which enabled subsequent fluorescent-activated cell sorting (FACS) and bulk gene expression analyses via RNA sequencing (RNA-seq). A connectivity score was calculated from the TM-connected versus TM-unconnected glioma cell subpopulations and applied to single-cell RNA-seq cluster analyses of unambiguously identified malignant cells from surgical specimens of human astrocytoma (see Supplementary Methods). We found that the previously described ApoE-positive cluster[16] had a significantly higher connectivity index, which suggests that this distinct tumour cell cluster is functionally related to the formation or maintenance of TM-connected cells (Extended Data Fig. 4m, n, Supplementary Table 4). In turn, this molecular marker of intratumoural connectivity strongly correlated with the expression of the AMPAR subunit GluA1 (Fig. 2f, Extended Data Fig. 4o). Together, these results suggest that the subpopulation of strongly TM-connected glioma cells, known drivers of incurable gliomas[10–12], shows molecular features of functional AMPAR-containing synaptic contacts. Accordingly, genes involved in neurogenesis pathways and synaptic processes were upregulated in certain ApoE-positive clusters in human IDH-mutated astrocytomas and GBs (Extended Data Fig. 4p, q, Supplementary Tables 5, 6).

AMPAR-mediated currents in tumour cells

We next characterized the functional properties of NGS in different model systems, starting with surgically removed tissue obtained from patients with glioblastoma (Fig. 3a). GB cells were identified by preoperative application of 5-aminolevulinic acid, which resulted in red fluorescence specifically in tumour cells (Fig. 3b, Supplementary Discussion 1.10). Targeted patch-clamp recordings revealed spontaneous excitatory postsynaptic currents (sEPSCs), thus demonstrating the existence of functional NGS in the human disease (Fig. 3c). We further investigated the functional properties of NGS in more accessible experimental model systems, taking advantage of GB cells that stably express GFP or tdTomato for their identification (Extended Data Fig. 5a). We also found sEPSCs in acute brain slices of xenografted mice, and human GB cells co-cultured with neurons (Fig. 3d). In all human samples and disease models studied, sEPSCs showed comparable amplitudes, rise times and decay kinetics, consistent with established values for glutamatergic synapses[23,24] (Extended Data Fig. 5b–d). To confirm the functional contribution of AMPARs, we applied the AMPAR antagonist cyanquixaline (CNQX) to co-cultures of GB cells and neurons and found that sEPSCs were strongly inhibited (Fig. 3e, Extended Data Fig. 5e). As shown above, the AMPAR subunit GluA2 is underedited in GB cells, potentially rendering AMPARs calcium-permeable. Therefore, we tested for the presence of functional calcium-permeable AMPARs in GB cells using the selective blocker 1-naphthyl acetylspermine (NASPM). We observed a marked decrease in sEPSCs (Extended Data Fig. 5f), which suggests that sEPSCs include currents mediated by calcium-permeable AMPARs. In addition to fast sEPSCs,

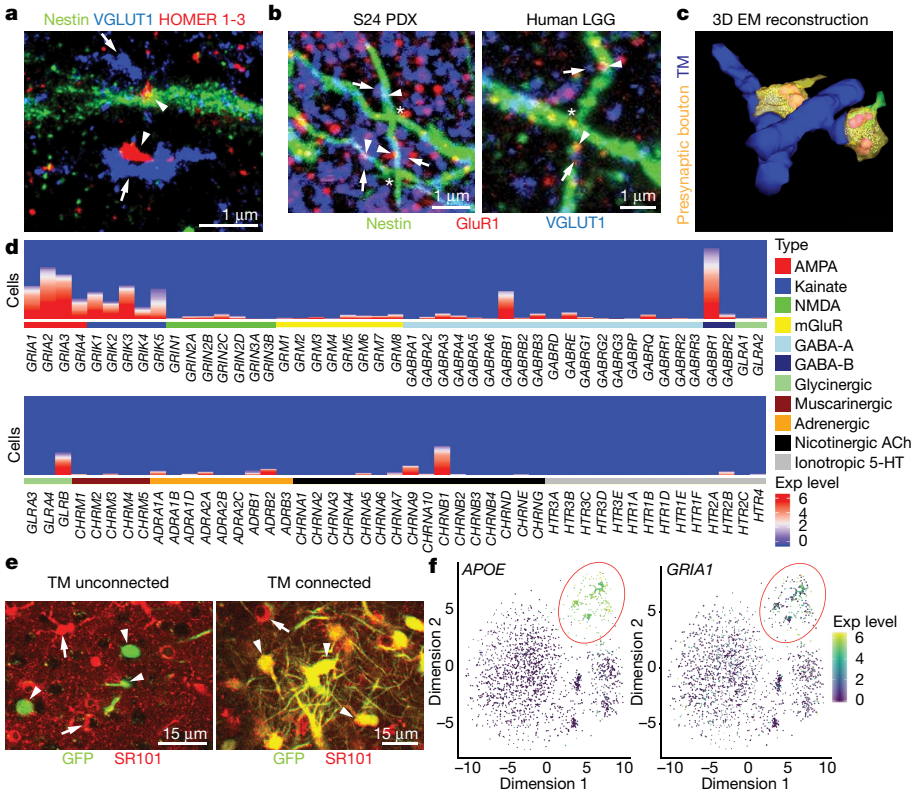

Fig. 2 | Molecular composition of NGS. a, Triple-colour 3D *d*STORM microscopy of a S24 PDX glioma TM ($n = 3$ experiments, 8 TMs identified with glutamatergic synapses). Arrows depict presynapses; arrowheads denote postsynapses. **b**, Confocal maximum intensity projection (MIP; 3-µm thick) of S24 PDX ($n = 5$ independent experiments) and human LGG (IDH(R132H) astrocytoma, $n = 2$ independent experiments). Arrows denote VGLUT1-stained vesicles; arrowheads denote postsynaptic GluR1 at sites where two different TMs crossed each other (asterisks)—a probable site for TM-connecting gap junctions. **c**, 3D electron microscopy reconstruction of images in Extended Data Fig. 4k showing presynaptic boutons (sepia), TMs (blue), presynaptic mitochondria (red) and a normal dendrite (green). **d**, Neurotransmitter receptor gene expression in single GB cells as determined by RNA-seq ($n = 4$ patients). Fifty per cent of all sequenced cells are depicted. **e**, In vivo MPLSM of uptake of the fluorescent dye SR101 from two fields of view (FOVs) ($n = 3$ experiments in 3 mice). **f**, *t*-distributed stochastic neighbour embedding (*t*-SNE) analysis (see Supplementary Methods) of IDH-mutated astrocytoma single-cell RNA-seq data ($n = 1{,}911$ single cells from 4 patients with IDH-mutated astrocytomas), with colour-coding of *APOE* (left) and *GRIA1* (right) expression levels shown.

we found spontaneous slow inward currents (SICs) in co-cultures of GB cells with neurons and acute brain slices of xenograft models (Fig. 3f, Extended Data Fig. 5g–n, Supplementary Discussion 1.11). These currents were markedly slower than sEPSCs (Extended Data Fig. 5g). To examine the conductances that underlie SICs more systematically, we electrically stimulated co-cultures to obtain evoked SICs.

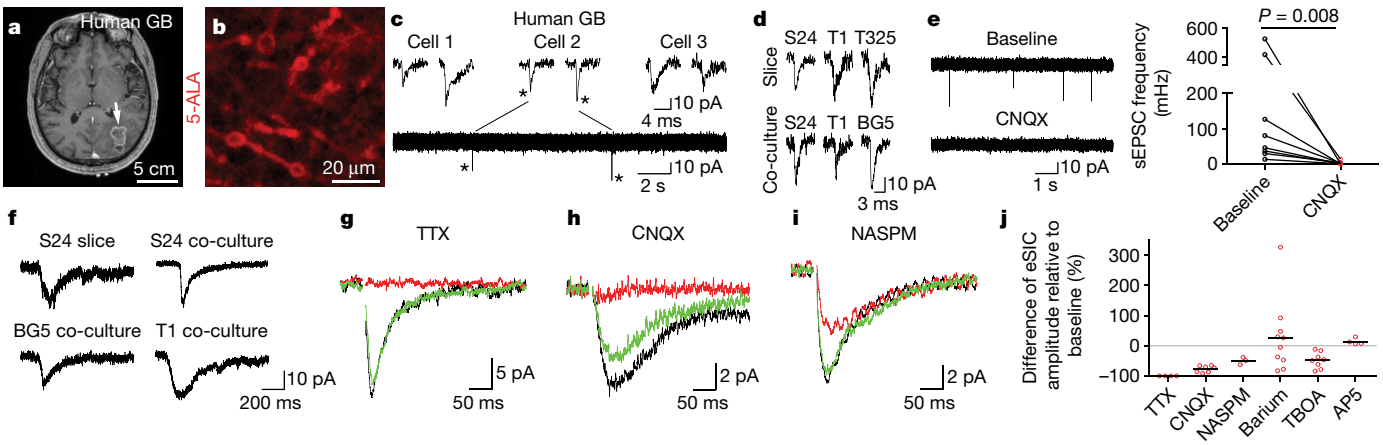

Fig. 3 | NGS are functional synapses. a, T1-weighted contrast-enhanced MRI image of a patient with GB who received 5-aminolevulinic acid (5-ALA) preoperatively. **b**, Acute brain slices of tissue from patient in **a** containing labelled GB cells (note spared nuclei; slices were obtained from $n = 4$ patients). **c**, Top, example sEPSCs ($n = 11$ analysed) recorded from three human GB cells. Bottom, overview trace of cell 2 with asterisks marking corresponding sEPSCs. **d**, Representative sEPSCs recorded in acute slices of different PDX cell lines (top) and co-cultures (bottom) (see 'Statistics and reproducibility' of Supplementary Methods for sample size). **e**, Application of CNQX to S24 cell co-culture and quantification ($n = 8$ cells). *P* value determined by two-sided Wilcoxon matched pairs test. **f**, Representative traces showing spontaneous SICs in different models. **g–i**, Pharmacology of evoked SICs in S24 co-culture (black denotes baseline; red denotes drug; green denotes washout). Stimulation artefact excluded from traces. NASPM, 1-naphthylacetyl spermine; TTX, tetrodotoxin. **j**, Quantification of drug effects on evoked SICs (eSICs) (TTX $n = 4$, CNQX $n = 7$, NASPM $n = 3$, barium $n = 10$, TBOA $n = 8$, and AP5 $n = 4$ biologically independent experiments). Grey line denotes 0% effect.

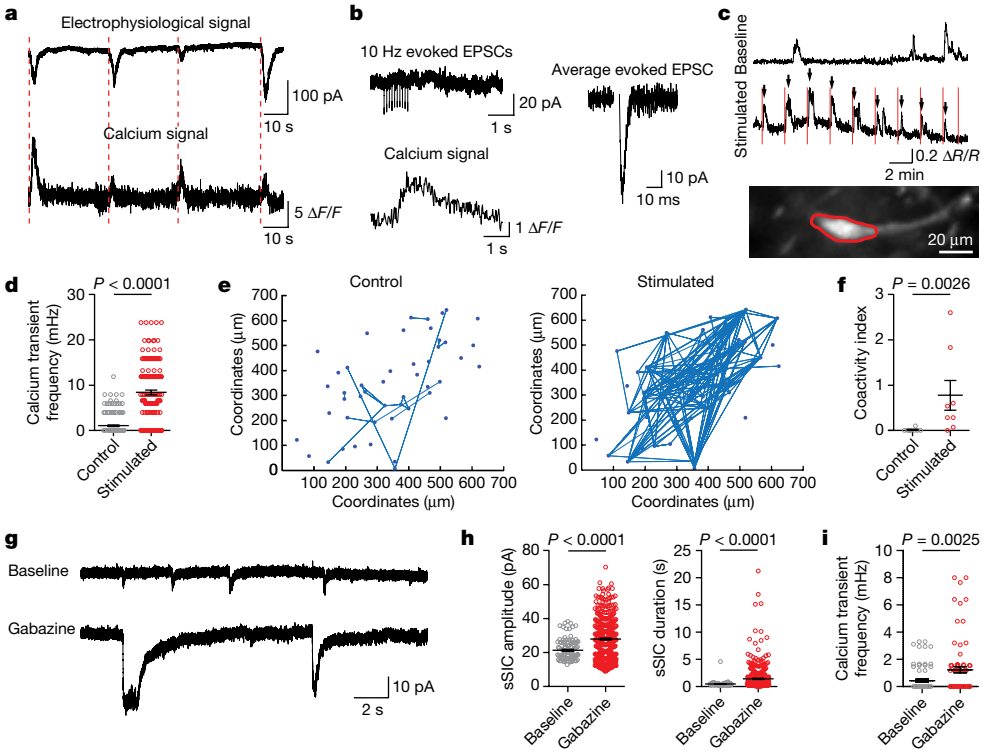

Fig. 4 | Neuronal input induces coordinated calcium transients in glioma networks. a, Top, representative whole-cell patch-clamp recording of spontaneous SICs. Bottom, corresponding GCaMP6 fluorescence trace in S24 cells co-cultured with neurons. Dashed lines mark the beginning of spontaneous SICs. **b**, Top, representative recording of evoked EPSCs. Bottom, corresponding GCaMP6 fluorescence trace in S24 cells co-culture with neurons. Right, average of 30 eEPSCs. **c**, Top, representative calcium traces, baseline (top) and neuronal stimulation of ChR2 (20 Hz for 1 s, indicated by red lines; bottom). Bottom, MPLSM in vivo imaging showing MIP of the respective glioma cell. **d**, Calcium transient frequency in glioma cells after stimulation ($n = 164$ cells in 4 S24 PDX mice). **e**, Coactivity map of glioma cells in vivo before and after neuronal stimulation of ChR2. The number of connecting lines reflects connectivity. **f**, Coactivity index of baseline versus neuronal ChR2 stimulation ($n = 8$ experiments in 4 S24 PDX mice). **g**, Representative current traces showing SICs recorded in S24 cells co-cultured with neurons. **h**, Effect of gabazine on spontaneous SIC amplitude and duration ($n = 115$ baseline events and $n = 409$ events under gabazine from $n = 8$ cells). **i**, Frequency of calcium transients in glioma cells under gabazine-induced epileptic conditions ($n = 54$ cells in baseline and under gabazine in 4 S24 PDX mice). *P* values determined by two-sided Mann–Whitney test. Data are mean ± s.e.m.

Again, action potentials in neurons were required to produce evoked SICs (Fig. 3g, j). CNQX inhibited evoked SICs more strongly than NASPM, consistent with our observation that GluR2 subunits are not fully edited (Extended Data Fig. 4e, f). The incomplete effect of CNQX also suggests that conductances other than AMPARs may contribute to evoked SICs. To test this further, we examined the contribution of activity-dependent extracellular potassium accumulation by superfusing barium-containing solution and found heterogeneous effects with either inhibition or potentiation of evoked SICs (Extended Data Fig. 5o, Fig. 3j). The contribution of glutamate transporter currents[25] to evoked SICs was tested by applying DL-threo-β-benzyloxyaspartate (TBOA), which either inhibited currents moderately or had no effect (Extended Data Fig. 5p, Fig. 3j). Finally, a contribution of *N*-methyl-D-aspartate (NMDA) receptors was not evident after application of 2-amino-5-phosphonovalerate (AP5; Extended Data Fig. 5q, Fig. 3j). The heterogeneous effects of the drugs can be attributed to the well-known extensive molecular, anatomical and physiological heterogeneity of tumour cells in human gliomas[10,11,17,26,27], which is also found for AMPAR subunits expressed in glioblastoma cells (Extended Data Fig. 4d). Thus, SICs arise from combinations of multiple conductances with a prominent contribution of AMPARs and extracellular potassium accumulation, and a less pronounced contribution of glutamate transporter currents. Most likely depending on the molecular composition of the GB cells participating in the response, the fractional contribution of each component differs (Fig. 3j). We further considered whether gap junctions that join glioma cells into a tumour cell network[10] contribute to SICs. We found that the input resistance was significantly lower in cells with, than in cells without, spontaneous SICs (Extended Data Fig. 5r). Furthermore, these currents were markedly reduced after the inhibition of gap junctions with GAP26 and GAP27 (Extended Data Fig. 5s, t) and meclofenamate (Extended Data Fig. 5u, v, w), which suggests that a glioma network response contributes to SICs. The anatomical integration into glioma networks is highly heterogeneous between single GB cells[10], thereby adding to the overall heterogeneity of SICs.

To assess the relative contribution of EPSCs and SICs, we next analysed their relative frequency of occurrence. In some recordings we found both EPSCs and SICs (Extended Data Fig. 5x). In summary, about 31% of recorded GB cells did show either current, or both, with distinct subpopulations (Extended Data Fig. 5y). Together, this argues for a relevant albeit electrophysiologically heterogeneous functional input of NGS on GB cells.

NGS activate glioma networks

We next addressed the coupling of SICs and EPSCs in GB cells to intracellular calcium signals known to be central for intraglioma communication[10]. First, we simultaneously recorded glioma current responses and their corresponding calcium signals (Fig. 4a, Extended Data Fig. 6a–c, Supplementary Discussion 1.12). Trains of evoked EPSCs also gave rise to glioma calcium signals (Fig. 4b). In none of the GB cells across all models ($n = 318$ cells) could we elicit action potentials, which indicates that GB cells are not electrically excitable (Extended Data Fig. 6d). To investigate calcium signals further, we recorded calcium transients in a PDX model, using in vivo multiphoton laser scanning microscopy (MPLSM) through a cranial window. After optogenetic

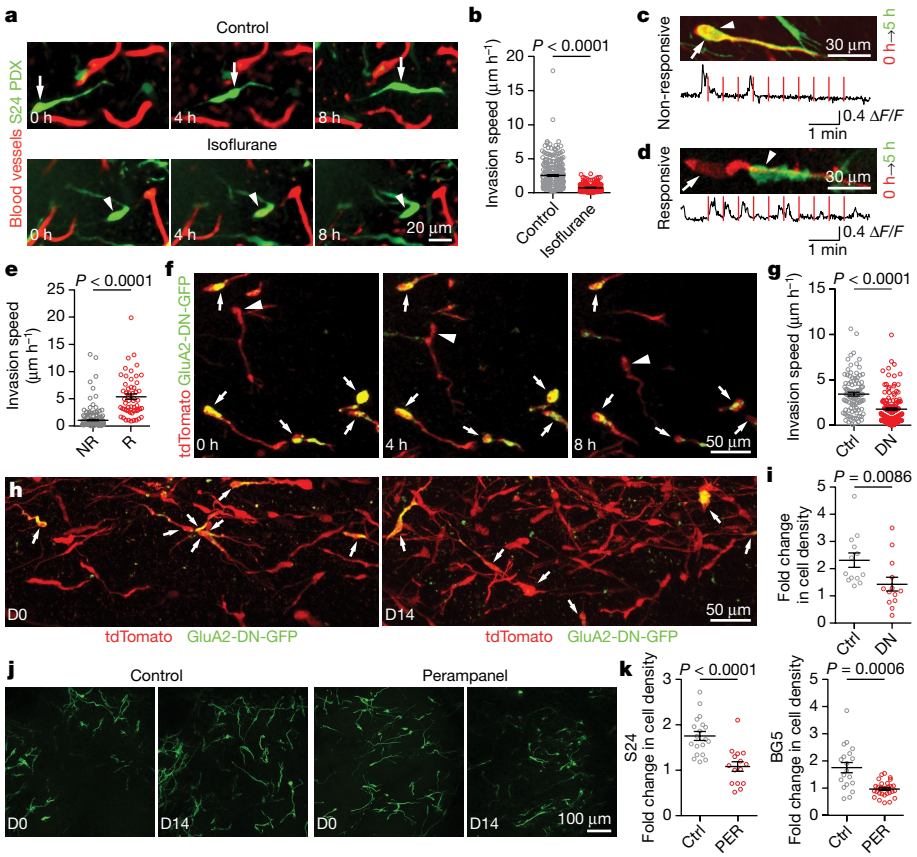

Fig. 5 | NGS drive brain tumour invasion and growth imaged in vivo. **a**, Representative time series of GB cells (green) and brain microvessels (red) under control conditions (arrows, 5 independent experiments in 4 mice) versus high-dose isoflurane (arrowheads, 4 independent experiments in 4 mice). **b**, Invasion speed of GB cells ($n = 254$ control cells versus $n = 143$ isoflurane cells in 4 S24 PDX mice). **c**, **d**, Representative time series of non-responsive (**c**) or responsive (**d**) S24 PDX GB cells (neuronal ChR2 stimulation (red lines); 9 independent experiments in 6 mice). Cells measured at 0 h (red; arrows) and at 5 h (green; arrowheads). **e**, Invasion speed of S24 PDX GB cells (non-responsive (NR) $n = 164$ cells in 5 mice; responsive (R) $n = 53$ cells in 5 mice). **f**, Representative time series showing glioma invasion of cells expressing Glu2A-DN-GFP and tdTomato (arrows) compared with glioma cells expressing only tdTomato (arrowheads). **g**, Invasion speed of GluA2-DN-GFP and tdTomato cells compared with control (Ctrl) cells (DN $n = 114$, Ctrl $n = 94$, 5 mice). **h**, Representative images of S24 xenografts, with GB cells expressing either GluA2-DN-GFP together with tdTomato (arrows) or only tdTomato at 0 and 14 days. **i**, Cell density changes over 14 days ($n = 13$ regions in 5 mice). **j**, Glioma regions on days 0 and 14 under control conditions and after treatment with the AMPAR antagonist perampanel. **k**, Cell density on day 14 versus day 0 under control versus perampanel (PER) conditions in two different PDX cell lines (S24: $n = 19$ control and $n = 15$ perampanel FOVs in 6 mice each; BG5: $n = 25$ control and $n = 29$ perampanel FOVs in 5 (control) and 6 mice (perampanel)). *P* values determined by two-sided Mann–Whitney test (**b**, **e**, **g**, **i**) or two-sided unpaired *t*-test with Welch's correction (**k**). Data are mean ± s.e.m.

stimulation of neurons transduced with channelrhodopsin-2 (ChR2) in a tumour-bearing brain region, GB cells showed increased calcium transient frequencies and synchronised calcium activity patterns, greatly exceeding the frequency of spontaneous calcium transients and spontaneous glioma network activity (Fig. 4c, d, Supplementary Video 5). We analysed the calcium transient frequency and network connectivity of GB cells by comparing calcium imaging time series of the same length before and after blue laser illumination that triggers synchronised neuronal activity. Evidently, the number of coactive GB cells increased strongly after ChR2 stimulation (Fig. 4e, f). Further analysis revealed that temporal heterogeneity exists with respect to the calcium response after neuronal activation, as illustrated by a cascade of peaks in vivo as well as in co-culture (Extended Data Fig. 6e–g), which suggests that a subpopulation of synaptically stimulated GB cells is able to transmit calcium waves to the remaining TM-connected glioma network. This is supported by an increased connectivity of functionally neuron-connected glioma cells compared with non-connected glioma cells after stimulation of ChR2 (see Supplementary Methods, Extended Data Fig. 6h, i) and consistent with the previously reported dependence of intercellular calcium waves on TM interconnections in these glioma models[10].

Epileptic seizures are a frequent clinical problem in patients with GB[28,29]. Epileptiform activity induced by gabazine resulted in potentiated SICs (Fig. 4g, h, Extended Data Fig. 6j) and subsequent calcium transients in GB cells (Fig. 4i). By contrast, deep anaesthesia with isoflurane, as regularly applied to patients during brain tumour surgery, or with a mixture of fentanyl, midazolam and medetomidine, inhibited the frequency of calcium transients and reduced the coordinated GB cell calcium activity in the neocortex in a dose-dependent and reversible manner (Extended Data Fig. 7a–h, Supplementary Videos 6, 7, Supplementary Discussion 1.12).

In summary, these data suggest that calcium can enter GB cells via AMPARs and possibly additional conductances, and that neuronal activity can cause time-locked and clinically relevant calcium signals in GB cell networks.

Neural activity drives glioma invasion

We next sought to clarify the biological consequences of NGS input with regard to GB cell invasion and proliferation—the two key components of tumour progression in this disease. Recording GB cell invasion velocity by repetitive in vivo imaging over 8 h, we found that isoflurane anaesthesia reduces the invasion speed of the rapidly invading tumour cells possessing TM extensions[11] (Fig. 5a, b, Extended Data Fig. 7i). Likewise, the subpopulation of GB cells that was functionally connected to neurons in vivo as detected by calcium responses to neuronal activation was significantly more invasive than

other GB cells (Fig. 5c–e). We further examined the relationship of calcium transients and GB cell movement by simultaneously imaging calcium and cell movement in co-cultures with neurons. Here, episodes of tumour cell migration correlated with the frequency of calcium signals (Extended Data Fig. 7j, k), supporting a causal link. Finally, to differentiate the effect of AMPAR function and hence NGS input on GB cell biology from other potential neuronal and non-neuronal factors, we expressed a dominant-negative AMPAR subunit (GluA2-DN) fused with green fluorescent protein (GluA2-DN-GFP; see Supplementary Methods; Extended Data Fig. 7l–p). When AMPAR signalling was thus genetically perturbed, in vivo GB cell invasion was reduced (Fig. 5f, g, Extended Data Fig. 7q). Together, several lines of evidence support a direct influence of NGS-driven, calcium-dependent activation of GB cells on GB cell invasion. Notably, recent work has shown that transient glutamatergic synapses also form on immature neurons during brain development, and drive their transition to a bipolar morphology and subsequent fast migration[30].

NGS stimulate tumour growth

To investigate whether proliferation of tumour cells and finally overall glioma progression is influenced by NGS, GB cells were transduced with an optogenetic construct to mimic synaptic stimulation (Extended Data Fig. 8a) using in vitro monocultures. Here, light stimulation led to a proliferative response of tumour cells (Extended Data Fig. 8b). Using intravital microscopy, we found that GB cells that express GluA2-DN-GFP co-transduced with tdTomato showed significantly reduced in vivo growth kinetics compared with AMPAR-unperturbed GB cells that express tdTomato, yet similar growth kinetics were observed in monocultures in vitro (Fig. 5h, i, Extended Data Fig. 8c). Dependency of the growth-inhibitory effects of AMPAR blockade on the presence of neurons was confirmed in vitro (Extended Data Fig. 8d–h). Furthermore, in a similar assay, both synaptically driven glutamate release (blocked by tetrodotoxin (TTX)), and non-synaptic glutamate release via cystine/glutamate exchange (inhibited by sulfasalazine (SAS)) were strongly involved in the pro-proliferative effects of glutamate on glioblastoma cells, with maximum effects in combination treatments—albeit only in co-culture with neurons, not in monoculture conditions (Extended Data Fig. 8i, j). This confirms that NGS are a distinct source of pro-proliferative glutamate activity for GB cells, independent of the additional paracrine and potential autocrine glutamate and neuroligin-3 effects that have been previously described[6,31] (Extended Data Fig. 8k–m, Supplementary Discussion 1.13).

The selective non-competitive AMPAR antagonist perampanel is an approved antiepileptic drug shown to have potential antitumour effects in patients with glioma and warrants further investigation[32]. Chronic administration of perampanel to xenografted mice decreased the proliferation of GB cells as determined by in vivo imaging of tumour regions over time (Fig. 5j, k, Extended Data Fig. 9a) independently of cell-autonomous effects as determined by an in vitro proliferation assay (Extended Data Fig. 9b).

In summary, blockade of NGS-driven synaptic communication between neurons and GB cells via genetic and pharmacological blockade of AMPAR signalling reduced GB cell malignancy, leading to attenuated glioma progression. This is supported by the functional importance of NGS in incurable paediatric gliomas[33].

Conclusions

The functionally relevant NGS reported here support the concept that hijacking mechanisms of normal CNS development and plasticity are key characteristics of incurable gliomas, particularly GBs[2,3,8,9]. During normal brain development and function, glutamatergic neurons can elicit circuit-specific responses from different stem-cell populations, including neuronal[30] and oligodendrocyte precursor cells[34], via functional synapses formed between neurons and these cell types. Clinically, most patients with incurable gliomas have epileptic seizures[29], and the reappearance or exacerbation of epileptic seizures is associated with tumour recurrence in malignant gliomas[26]. Although this has been classically explained by tumour growth itself[35], a reverse causality has recently been suggested: excessive neuronal activity during seizures might actually stimulate brain tumour progression[36]. Here we describe a morphological and functional basis for this observation with potential clinical consequences. Glutamatergic neurogliomal synapses, partially via their influence on calcium communication in TM-connected tumour cell networks, drive the progression of brain tumours by stimulating glioma invasion and growth (Extended Data Fig. 10). The discovery of these complex glioma circuit dynamics makes modulators of synaptic transmission—such as the clinically approved AMPAR-inhibiting antiepileptic drug perampanel—particularly interesting candidates for further preclinical studies and clinical trials in neurooncology.

Reporting summary

Further information on research design is available in the Nature Research Reporting Summary linked to this paper.

Data availability

Bulk RNA-seq data have been deposited in the Sequence Read Archive (SRA) database under the accession number PRJNA554870. Clinical data of patient samples can be found in Supplementary Table 2. All other data and code that support the findings of this study are available from the corresponding authors on reasonable request.

Code availability

Custom-written MATLAB and Igor code is available upon reasonable request.

Online content

Any methods, additional references, Nature Research reporting summaries, source data, extended data, supplementary information, acknowledgements, peer review information; details of author contributions and competing interests; and statements of data and code availability are available at https://doi.org/10.1038/s41586-019-1564-x.

Received: 28 September 2018; Accepted: 9 August 2019;
Published online 18 September 2019.

1. Scherer, H. J. A critical review: the pathology of cerebral gliomas. *J. Neurol. Psychiatry* **3**, 147–177 (1940).
2. Venkatesh, H. S. et al. Neuronal activity promotes glioma growth through neuroligin-3 secretion. *Cell* **161**, 803–816 (2015).
3. Venkatesh, H. S. et al. Targeting neuronal activity-regulated neuroligin-3 dependency in high-grade glioma. *Nature* **549**, 533–537 (2017).
4. Ishiuchi, S. et al. Blockage of Ca^{2+}-permeable AMPA receptors suppresses migration and induces apoptosis in human glioblastoma cells. *Nat. Med.* **8**, 971–978 (2002).
5. Takano, T. et al. Glutamate release promotes growth of malignant gliomas. *Nat. Med.* **7**, 1010–1015 (2001).
6. Savaskan, N. E. et al. Small interfering RNA-mediated xCT silencing in gliomas inhibits neurodegeneration and alleviates brain edema. *Nat. Med.* **14**, 629–632 (2008).
7. Rzeski, W., Turski, L. & Ikonomidou, C. Glutamate antagonists limit tumor growth. *Proc. Natl Acad. Sci. USA* **98**, 6372–6377 (2001).
8. Li, L. & Hanahan, D. Hijacking the neuronal NMDAR signaling circuit to promote tumor growth and invasion. *Cell* **153**, 86–100 (2013).
9. Li, L. et al. GKAP acts as a genetic modulator of NMDAR signaling to govern invasive tumor growth. *Cancer Cell* **33**, 736–751 (2018).
10. Osswald, M. et al. Brain tumour cells interconnect to a functional and resistant network. *Nature* **528**, 93–98 (2015).
11. Jung, E. et al. Tweety-homolog 1 drives brain colonization of gliomas. *J. Neurosci.* **37**, 6837–6850 (2017).
12. Weil, S. et al. Tumor microtubes convey resistance to surgical lesions and chemotherapy in gliomas. *Neuro-oncol.* **19**, 1316–1326 (2017).
13. Zhu, Z. et al. Targeting self-renewal in high-grade brain tumors leads to loss of brain tumor stem cells and prolonged survival. *Cell Stem Cell* **15**, 185–198 (2014).
14. Harris, K. M. & Weinberg, R. J. Ultrastructure of synapses in the mammalian brain. *Cold Spring Harb. Perspect. Biol.* **4**, a005587 (2012).
15. Gray, E. G. Axo-somatic and axo-dendritic synapses of the cerebral cortex: an electron microscope study. *J. Anat.* **93**, 420–433 (1959).
16. Venteicher, A. S. et al. Decoupling genetics, lineages, and microenvironment in IDH-mutant gliomas by single-cell RNA-seq. *Science* **355**, eaai8478 (2017).
17. Darmanis, S. et al. Single-cell RNA-seq analysis of infiltrating neoplastic cells at the migrating front of human glioblastoma. *Cell Reports* **21**, 1399–1410 (2017).

18. Maas, S., Patt, S., Schrey, M. & Rich, A. Underediting of glutamate receptor GluR-B mRNA in malignant gliomas. *Proc. Natl Acad. Sci. USA* **98**, 14687–14692 (2001).
19. Sommer, B., Köhler, M., Sprengel, R. & Seeburg, P. H. RNA editing in brain controls a determinant of ion flow in glutamate-gated channels. *Cell* **67**, 11–19 (1991).
20. Burnashev, N., Monyer, H., Seeburg, P. H. & Sakmann, B. Divalent ion permeability of AMPA receptor channels is dominated by the edited form of a single subunit. *Neuron* **8**, 189–198 (1992).
21. Dalva, M. B., McClelland, A. C. & Kayser, M. S. Cell adhesion molecules: signalling functions at the synapse. *Nat. Rev. Neurosci.* **8**, 206–220 (2007).
22. John Lin, C. C. et al. Identification of diverse astrocyte populations and their malignant analogs. *Nat. Neurosci.* **20**, 396–405 (2017).
23. Mosbacher, J. et al. A molecular determinant for submillisecond desensitization in glutamate receptors. *Science* **266**, 1059–1062 (1994).
24. Traynelis, S. F. et al. Glutamate receptor ion channels: structure, regulation, and function. *Pharmacol. Rev.* **62**, 405–496 (2010).
25. Bergles, D. E., Diamond, J. S. & Jahr, C. E. Clearance of glutamate inside the synapse and beyond. *Curr. Opin. Neurobiol.* **9**, 293–298 (1999).
26. Korber, V. et al. Evolutionary trajectories of IDH^{WT} glioblastomas reveal a common path of early tumorigenesis instigated years ahead of initial diagnosis. *Cancer Cell* **35**, 692–704.e612 (2019).
27. Patel, A. P. et al. Single-cell RNA-seq highlights intratumoral heterogeneity in primary glioblastoma. *Science* **344**, 1396–1401 (2014).
28. Chaichana, K. L., Parker, S. L., Olivi, A. & Quiñones-Hinojosa, A. Long-term seizure outcomes in adult patients undergoing primary resection of malignant brain astrocytomas. *J. Neurosurg.* **111**, 282–292 (2009).
29. Weller, M., Stupp, R. & Wick, W. Epilepsy meets cancer: when, why, and what to do about it? *Lancet Oncol.* **13**, e375–e382 (2012).
30. Ohtaka-Maruyama, C. et al. Synaptic transmission from subplate neurons controls radial migration of neocortical neurons. *Science* **360**, 313–317 (2018).
31. de Groot, J. & Sontheimer, H. Glutamate and the biology of gliomas. *Glia* **59**, 1181–1189 (2011).
32. Izumoto, S. et al. Seizures and tumor progression in glioma patients with uncontrollable epilepsy treated with perampanel. *Anticancer Res.* **38**, 4361–4366 (2018).
33. Venkatesh, H. et al. Electrical and synaptic integration of glioma into neural circuits. *Nature* https://doi.org/10.1038/s41586-019-1563-y (2019).
34. Gibson, E. M. et al. Neuronal activity promotes oligodendrogenesis and adaptive myelination in the mammalian brain. *Science* **344**, 1252304 (2014).
35. Buckingham, S. C. et al. Glutamate release by primary brain tumors induces epileptic activity. *Nat. Med.* **17**, 1269–1274 (2011).
36. Huberfeld, G. & Vecht, C. J. Seizures and gliomas-towards a single therapeutic approach. *Nat. Rev. Neurol.* **12**, 204–216 (2016).
37. Verhaak, R. G. et al. Integrated genomic analysis identifies clinically relevant subtypes of glioblastoma characterized by abnormalities in PDGFRA, IDH1, EGFR, and NF1. *Cancer Cell* **17**, 98–110 (2010).

Acknowledgements We thank M. Kaiser, S. Hoppe, J. Grosch, S. Weil, I. Sonntag, M. Osswald, K. Gunkel, C. Kocksch, I. Frommer, A. Schlicksupp, R. Rosauer, H.-Y. Nguyen, L. Doerner, M. Schmitt, U. Lindenberger, H. Zheng and S. Wendler for scientific discussion, support and assistance. We thank A. Hotz-Wagenblatt for help with bioinformatic analysis pipelines. We thank M. Suva and I. Tirosh for support with the analysis of single-cell RNA-seq databases from human gliomas, C. Steinhäuser and R. Jabs for advice on how to perform electrophysiological recordings from non-neuronal postsynaptic cells and the EM Core Facility of University Heidelberg for general support. We thank M. Monje for stably transducing our S24 glioma cell line with ChR2(H134R). We thank C. Watts for generating and providing the E2 primary glioblastoma cell line. A.A. was supported by the Chica and Heinz Schaller research foundation and the grant from the Deutsche Forschungsgemeinschaft (AG 287/1-1). V.V. was supported by the MD/PhD program of the Medical Faculty Heidelberg and the Stiftung für Krebs- und Scharlachforschung. D.I.T. was supported by the Deutsche Krebshilfe. W.W. and F.W. were supported by a grant from the Deutsche Forschungsgemeinschaft (SFB 1389). F.W. was supported by a grant from the Deutsche Forschungsgemeinschaft (WI 1930/6). T. Kuner was supported by the CellNetworks Excellence Cluster (EXC 81). F.W. and T. Kuner acknowledge their children Jakob and Manili, respectively, for seeding this collaboration.

Author contributions V.V., F.W. and T. Kuner conceptualized and supervised the study, interpreted the data, and wrote the manuscript with the input of all co-authors. V.V. performed experiments and contributed to all aspects of the study, in particular electron microscopy, super-resolution microscopy, simultaneous calcium imaging and electrophysiology, expression analysis, in vivo multi-photon microscopy of glioma network activity, proliferation and invasion and the perampanel study. V.V. initially discovered the ultrastructural correlate of NGS. D.I.T. performed electrophysiological recordings of human tissue, ex vivo and co-culture, as well as electrophysiological recordings with simultaneous calcium imaging, epilepsy experiments, and analysed data. C.S. performed electrophysiological recordings as well as electrophysiological recordings in combination with calcium imaging, neuroglioma co-cultures, proliferation assays, built and programmed the in vitro optogenetics setup and analysed data. A.S.-F. performed cranial window implantation, in vivo two-photon microscopy, epilepsy experiments, and analysed data. L.F. performed cranial window implantation, in vivo two-photon microscopy, performed in vitro experiments and analysed data. T. Kessler performed bioinformatic analysis of RNA-expression data. C.K. performed initial electrophysiological recordings from xenografted glioma cells in brain slices and supervised subsequent electrophysiology. M.K. performed 3D electron microscopy reconstructions. R.X. performed SR101 experiments and subsequent analysis. H.H. provided electron microscopy of co-cultured NGS and technical advice. M.M. performed initial perampanel experiments with in vivo two-photon microscopy. M.R. provided tissue from tumour surgery. S.P.P. performed in vitro experiments and analysed data. J.K. provided advice for in vivo two-photon microscopy. F.S. provided stainings from human paraffin sections. F.T.K. provided MRI images. A.A.A. provided the syngeneic model. F.H. helped with analysis of glioma network activity. A.A. and D.E.B. provided plasmids encoding the dominant-negative GluA2 subunit fused to GFP. S.T. provided the oligodendroglioma cell line. C.M. provided the meningioma cell line. A.C. and H.M. provided the GBSC lines E2 and BG5. D.H. provided tissue from tumour surgery. H.-K.L. provided the syngeneic model. W.W. provided conceptual input, performed data interpretation and supervised RNA-expression data analysis.

Competing interests F.W. and W.W. are inventors of the patent WO2017020982A1 'Agents for use in the treatment of glioma'. This patent covers new treatment strategies that all target the formation and function of TMs in glioma. F.W. reports research collaboration with DC Europa Limited, Glaxo Smith Kline, Genentech and Boehringer.

Additional information

Supplementary information is available for this paper at https://doi.org/10.1038/s41586-019-1564-x.

Correspondence and requests for materials should be addressed to V.V., F.W. or T.K.

Peer review information *Nature* thanks Andrés Barría, Michael Taylor and the other, anonymous, reviewer(s) for their contribution to the peer review of this work.

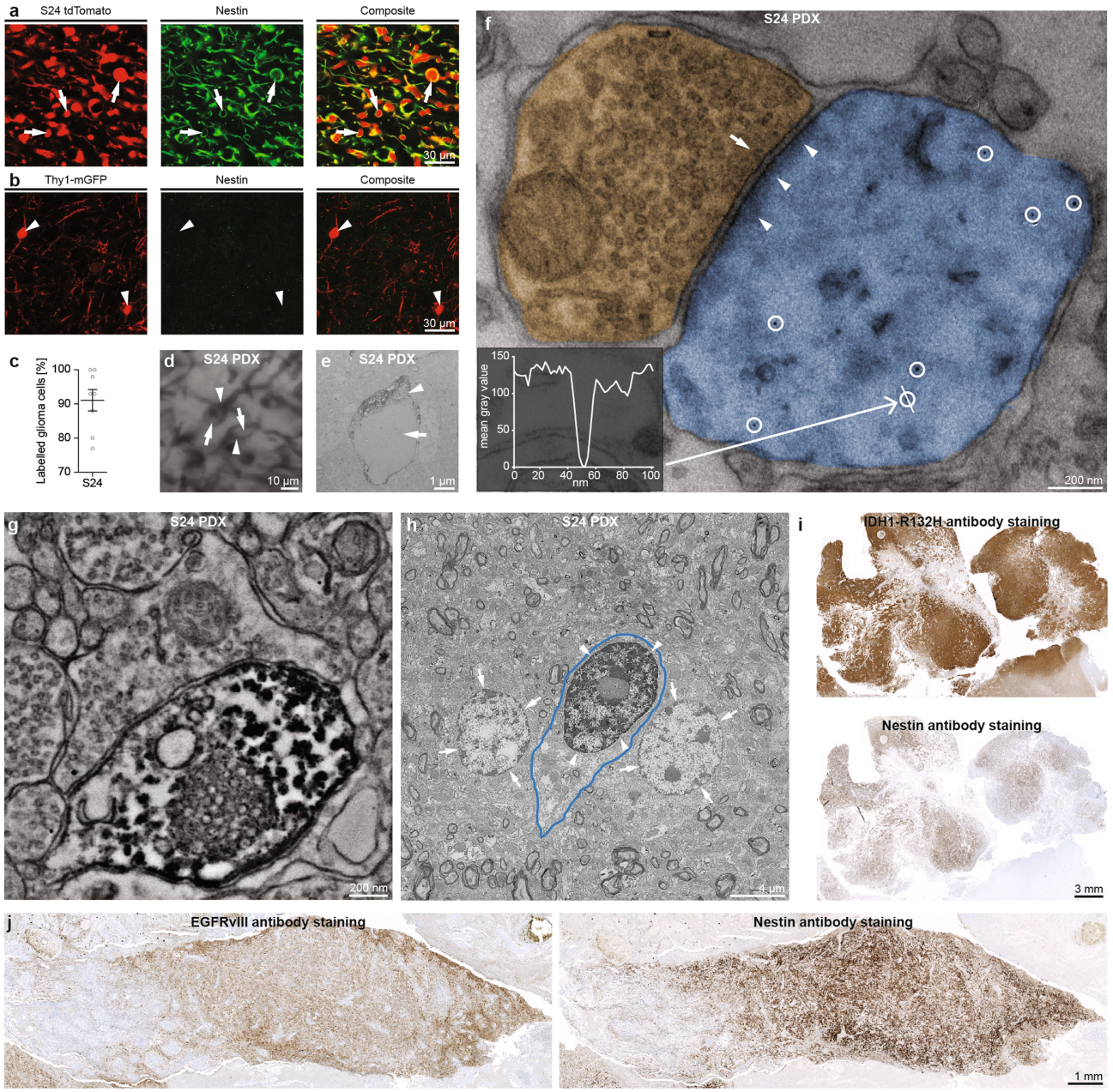

Extended Data Fig. 1 | Sensitivity and specificity of staining methods to detect glioma cells, TMs and NGS. a, S24 PDX cells constitutively expressing tdTomato, co-labelled with a human epitope-specific antibody against nestin, with the latter sparing the nucleus (arrows). **b**, Nestin labelling is not detectable in Thy1-mGFP mice that express monomeric green fluorescent protein (mGFP) in a subset of neurons (arrowheads). **c**, On average, more than 90% of glioma cells in the S24 xenograft model are nestin-positive ($n = 5$ samples of 3 mice). **d**, **e**, Nestin specifically labels somata and TMs excluding the nucleus as revealed by DAB labelling using wide-field light microscopy (**d**) and transmission electron microscopy (**e**) (see Fig. 1f and Extended Data Fig. 2a–d for sample sizes). Arrowheads denote DAB-positive cytosolic regions of cells; arrows arrows denote DAB-spared nuclei. **f**, Immunogold labelling of a nestin-positive glioma TM (blue) in a S24 PDX mouse ($n = 13$ samples in 2 mice). Sepia staining denotes presynaptic bouton. Circles denote 5-nm immunogold particles, with an associated line profile through a 5-nm immunogold particle (bottom left) illustrating its high electron density. Arrowheads denote postsynaptic density of an asymmetric synaptic contact; arrow denotes docked vesicle at the active zone. **g**, Electron micrograph of an exemplary NGS as depicted in Fig. 1a, showing the electron-dense precipitate without colouring (see Fig. 1f for sample size). **h**, Nuclear DAB precipitate in a glioma cell expressing histone–GFP stained with an anti-GFP antibody ($n = 3$ samples in 2 mice). After DAB precipitation, the nucleus is prominently more electron-dense (arrowheads) than the nuclei from neighbouring non-malignant cells (arrows). The cell is outlined by a blue line. **i**, Nestin specifically labels glioma cells in IDH1(R132H)-mutated human gliomas. Glioma cells are unambiguously identified with the IDH1(R132H)-specific antibody. Nestin was stained on an adjacent section. The anti-nestin antibody specifically labels large subsets of IDH-positive areas. Nestin-positive microregions that are negative for IDH1(R132H) are not detectable ($n = 3$ patient samples). **j**, Immunostaining as in **i**, with an anti-EGFRvIII tumour-cell-specific antibody in wild-type IDH human GB, confirming the high degree of specificity of nestin staining that is only detectable in brain microregions that contain tumour cells ($n = 3$ patient samples). EGFRvIII denotes deletion variant III of EGFR. Data are mean ± s.e.m.

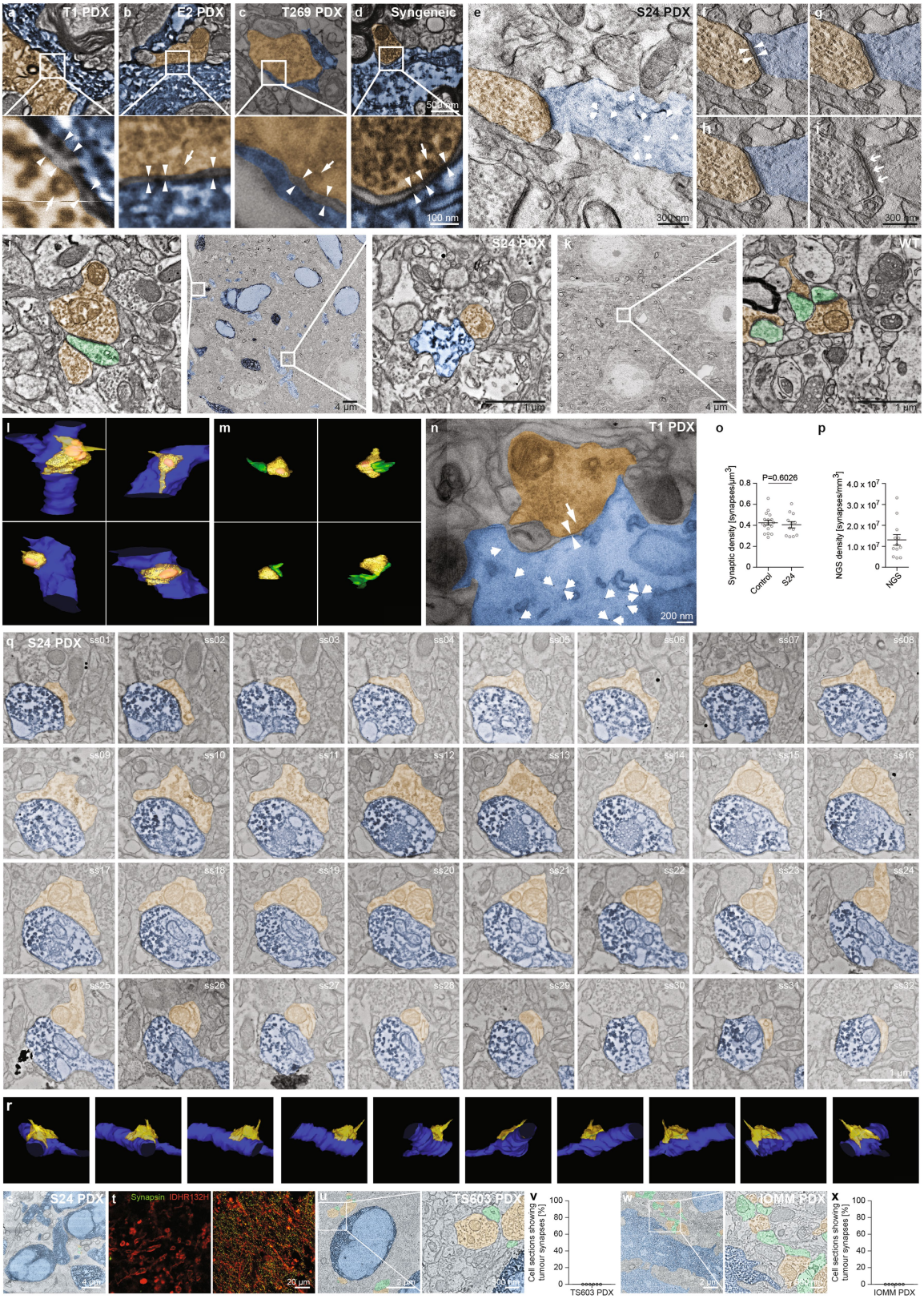

Extended Data Fig. 2 | See next page for caption.

Extended Data Fig. 2 | Ultrastructural identification of NGS across models. a–**d**, Immuno-electron microscopy images of NGS in different mouse glioma models. Ultrastructural NGS identification with an anti-human nestin antibody and consecutive DAB precipitate in T1 PDX (**a**, $n = 3$ tissue blocks in 3 mice), E2 PDX (**b**, $n = 5$ tissue blocks in 1 mouse), T269 PDX (**c**, $n = 3$ tissue blocks in 1 mouse) and with an anti-GFP antibody and consecutive DAB precipitation in the syngeneic mouse glioma model where tumour cells express GFP (**d**, $n = 5$ samples in 3 mice). Arrowheads denote the synaptic cleft; arrows denote docked vesicles. Scanning electron microscopy (SEM) (**a**, **b**, **d**) and transmission electron microscopy (TEM) (**c**) images are shown. **e**, Electron tomography showing an overview of S24 PDX NGS with glioma cells marked by the anti-nestin antibody and consecutive 5-nm immunogold labelling. Arrows denote immunogold particles (8 tomograms from 2 S24 mice). **f**–**i**, Serial virtual 20-nm sections of **e** through the active zone of a NGS. In **i**, arrows denote postsynaptic density. Arrowheads denote the synaptic cleft. **j**, Overview electron microscopy image of S24 PDX marked by nestin and DAB precipitate, illustrating the infiltration zone of the tumour ($n = 12$ FOVs with a total area of approximately 13,400 μm^2 in 2 S24 mice were evaluated). All samples analysed in this study showing NGS were obtained from such infiltration zones. Magnifications show normal synapses (left) and NGS (right). **k**, Overview and magnification of wild-type cortex labelled with nestin ($n = 17$ FOVs with a total area of approximately 12,400 μm^2 in 2 wild-type mice were evaluated). As expected, in the absence of tumour cells, no DAB precipitate can be seen, indicating the tumour cell-specificity of the nestin staining in the analysed samples. **l**, Four examples of fully reconstructed NGS. **m**, Four fully reconstructed normal synapses located next to NGS. **n**, Immunogold labelling of nestin in T1 PDX (7 tissue blocks from T1 PDX from 3 mice). Small arrows depict immunogold particles; arrowheads point towards the synaptic cleft; long arrows denote docked vesicles. **o**, Stereologically determined synaptic density in wild-type neocortex and in glioma cell infiltration zone. No significant difference of the density of normal synapses could be found (two-sided unpaired *t*-test; $n = 12$ and 17 FOVs in 3 mice each). **p**, Stereologically quantified NGS density in the S24 PDX model ($n = 12$ FOVs in 2 S24 mice). **q**, Electron microscopy sections of a fully reconstructed NGS (representative example from $n = 66$ glioma and 52 healthy synaptic boutons in 3 samples from S24 mice). Consecutive serial sections are denoted ss01 to ss32. **r**, Different better view angles of the 3D reconstructed NGS from **q**. **s**, Electron microscopy image of the main tumour mass in the S24 PDX model showing no apparent NGS ($n = 2$ samples in 2 S24 mice). **t**, Immunofluorescence staining using an IDH1(R132H)-specific antibody (red) and a presynaptic bouton marker (synapsin, green) in the main tumour mass (left, $n = 3$ samples from 3 patients with IDH1(R132H)-mutated glioblastoma) and in the infiltration zone (right, $n = 3$ samples from 3 patients with IDH1(R132H)-mutated glioblastoma). **u**–**x**, Representative immuno-electron microscopy images of oligodendroglioma (**u**, **v**) and meningioma (**w**, **x**) PDX models. No neuron-tumour synapses were found ($n = 6$ samples TS603 with 361 oligodendroglioma cell sections from 3 mice and $n = 6$ samples IOMM with 309 meningioma cell sections from 3 mice were analysed). Data are mean ± s.e.m. Colour code in all panels: presynaptic boutons (sepia), glioma cell somata and TMs (blue), postsynaptic dendrites of neurons (green).

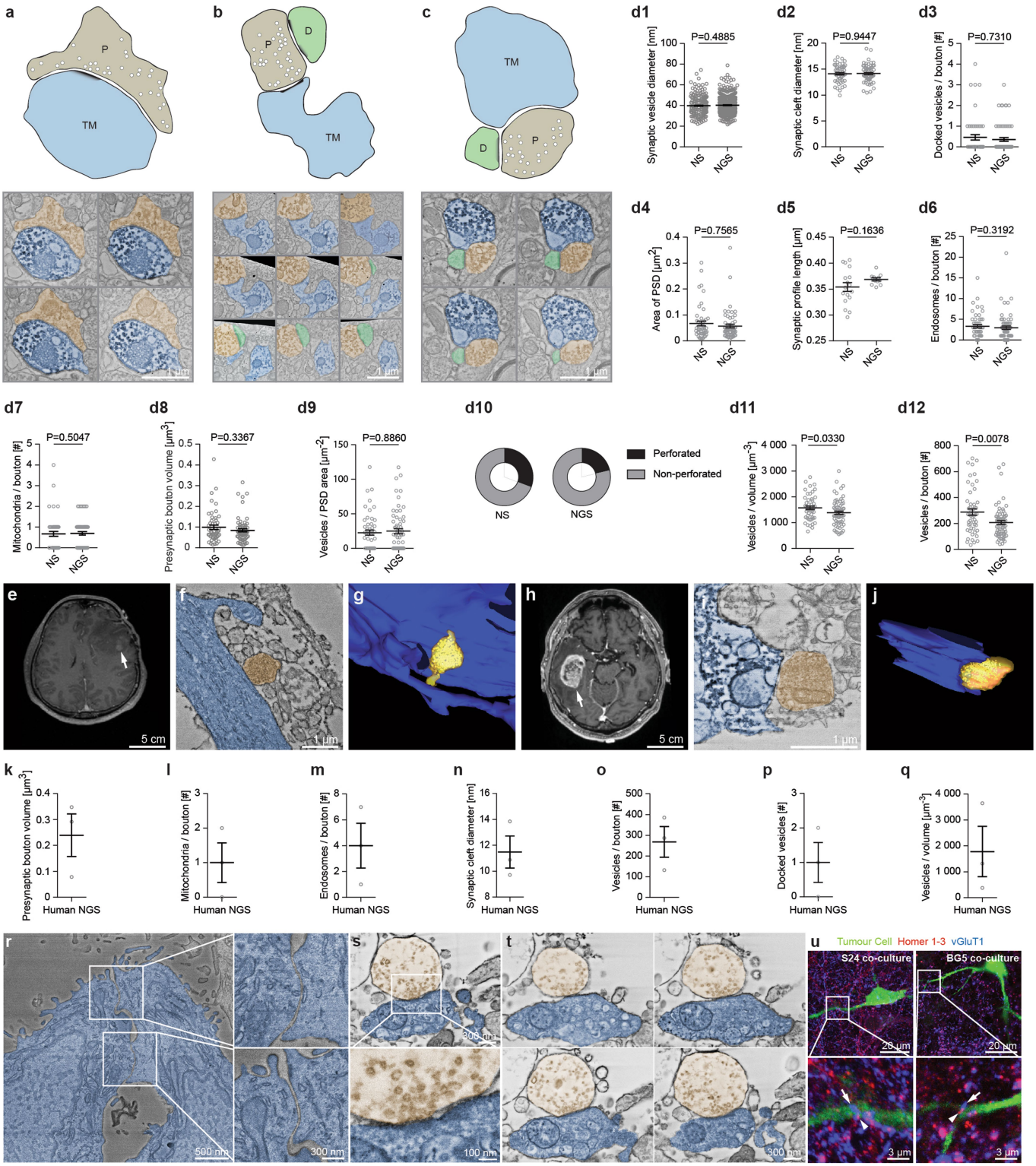

Extended Data Fig. 3 | See next page for caption.

Extended Data Fig. 3 | NGS classification in PDX glioma models and human tumour samples. a–**c**, Three different morphological categories of glioma TM-associated synaptic contacts: single synaptic contact on a glioma TM (**a**); multisynaptic contact to both a glioma TM and a neuron (**b**); and a TM approaching an existing neuronal synapse with contact to the synaptic cleft, but without showing ultrastructural details of a bona-fide NGS (**c**). The corresponding original data with serial electron microscopy sections are shown underneath the schematic drawings. **d1**–**d12**, Morphometric synaptic parameter quantification of normal brain synapses versus NGS. **d1**, Synaptic vesicle diameter. **d2**, Synaptic cleft diameter. **d3**, Number of docked vesicles per bouton. **d4**, Area of postsynaptic density (PSD). **d5**, Synaptic profile length. **d6**, Number of endosomes per bouton. **d7**, Number of mitochondria per bouton. **d8**, Presynaptic bouton volume. **d9**, Number of vesicles per PSD area. **d10**, Percentage of perforated versus unperforated synapses. Perforation refers to a hole formed within the PSD area. **d11**, Vesicles per volume. **d12**, Vesicles per bouton. In conclusion, NGS are morphometrically similar to neuronal synapses. (**d2**, **d5** two-sided unpaired *t*-test, **d1**, **d3**, **d4**, **d6**, **d7**, **d8**, **d9**, **d10**, **d11, d12** two-sided Mann–Whitney test; $n = 52$ normal synapses and $n = 66$ NGS). **e**, T1 gadolinium contrast-enhanced MRI image of a patient diagnosed with an IDH1(R132H)-mutated astrocytoma WHO grade II (arrow). **f**, Representative example of a NGS imaged with SEM in resected tumour material of the patient in **e**. **g**, Fully reconstructed 3D model of the NGS in **f**. **h**, T1 gadolinium contrast-enhanced MRI image of a patient diagnosed with wild-type IDH GB (arrow). **i**, Representative example of a NGS imaged with SEM in resected tumour material of the patient in **h**. **j**, Fully reconstructed 3D model of the NGS in **i**. **k**–**q**, Quantification of synaptic morphometry in three examples of fully reconstructed NGS in resected material from a patient with IDH1(R132H)-mutated astrocytoma WHO grade II. **k**, Presynaptic bouton volume. **l**, Number of mitochondria per bouton. **m**, Number of endosomes per bouton. **n**, Synaptic cleft diameter. **o**, Number of vesicles per bouton. **p**, Number of docked vesicles. **q**, Number of vesicles per volume. The synaptic morphometry of human NGS was comparable to normal synapses. **r**, SEM images of S24 GB cell spheroids showing no synaptic ultrastructural differentiations at contact sites (see Supplementary Data Table 3 $n = 8$ S24 spheroid blocks, $n = 3$ T1 spheroid blocks). **s**, Example of a SEM image of a co-culture of S24 GB cells with cortical neurons: NGS that can be found in glioma cells stained with a human-specific anti-nestin antibody with consecutive DAB precipitation ($n = 2$ samples). **t**, Serial sections of the NGS depicted in **s**. **u**, Confocal MIP images of 10 μm of glioma cell co-cultures with cortical neurons. Putative synaptic contacts in GBSC line S24 (left, $n = 12$ putative synapses) and GBSC line BG5 (right, $n = 8$ putative synapses) in two independent experiments. Arrowheads denote postsynaptic HOMER1–3 cluster; arrows denote presynaptic VGLUT1. Data are mean ± s.e.m. Colour code in **a**–**t**: presynaptic boutons (sepia), glioma cell somata and TMs (blue), postsynaptic dendrites of neurons (green).

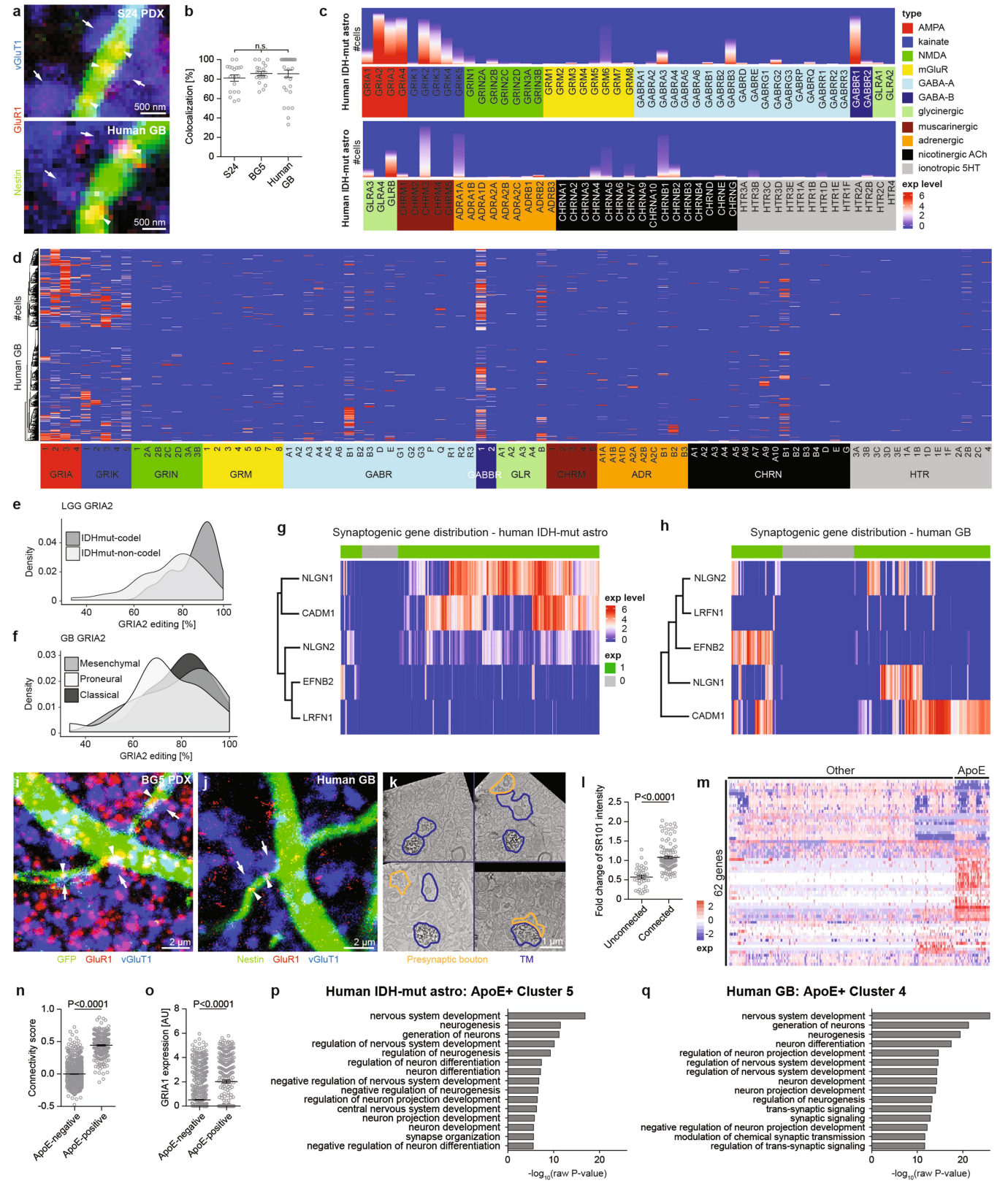

Extended Data Fig. 4 | See next page for caption.

Extended Data Fig. 4 | Extended molecular characterization of NGS. **a**, Confocal maximum intensity projection (900 nm) showing co-localization of AMPAR (GluR1, arrowheads) with TMs (nestin) and presynaptic glutamatergic boutons (VGLUT1, arrows) ($n = 3$ mice for S24 and $n = 3$ human GB samples, see **b**). **b**, Quantitative co-localization analysis for the S24 and BG5 PDX models and human GB ($n = 19$ FOVs with 248 clusters in 3 mice for S24 PDX, $n = 20$ FOVs with 384 clusters in 1 mouse for BG5 PDX, $n = 32$ FOVs with 215 clusters in 3 human GB samples). *P* values determined by two-sided Kruskal–Wallis test with post hoc Dunn's multiple comparisons test. **c**, Expression levels of neurotransmitter receptors detected by single-cell RNA-sequencing obtained from resected material of human IDH-mutated astrocytomas ($n = 4$ patients). **d**, Heat map with single-cell expression of neurotransmitter receptors in the single-cell glioblastoma dataset. Each column depicts a single cell. Glioblastoma cells are hierarchically clustered by receptor expression as depicted by the dendrogram. **e**, Chromosomal 1p/19q co-deletion and non-co-deletion determines classification into either IDH-mutated non-co-deleted astrocytomas or co-deleted oligodendrogliomas. Astrocytomas show significantly lower relative amount of *GRIA2* mRNA editing than 1p/19q co-deleted oligodendrogliomas ($n = 521$ patient samples). $P < 0.0001$, two-sided Mann–Whitney test. **f**, Relative level of *GRIA2* mRNA editing in human GBs according to their gene expression subtype[37] ($n = 60$ GB patient samples and 24 LGG patient samples). See Supplementary Table 7 for *P* values; ordinary one-way analysis of variance (ANOVA) with Tukey's multiple comparisons test. **g**, **h**, Single-cell expression analysis of synaptogenic genes in human IDH-mutated astrocytomas (**g**) and GBs (**h**). Most tumour cells express at least one of the five genes that have been most robustly associated with synaptogenesis (*NLGN1* (neuroligin 1), *NLGN2* (neuroligin 2), *LRFN1* (leucine-rich repeat and fibronectin type III domain-containing protein 1), *CADM1* (cell adhesion molecule 1) and *EFNB2* (ephrin B2)). The green colour on top of the graph indicates that at least one of the synaptogenic genes is expressed in the particular cell. Each vertical column represents one cell with the normalized expression of the synaptogenic genes. The order of the *x* axis is determined by hierarchical clustering without showing the dendrogram. **i**, **j**, Confocal MIP of 10 μm of the BG5 PDX model (**i**, $n = 3$ samples in 1 mouse) and human GB (**j**, $n = 3$ samples in resected material from 3 patients) demonstrating connections between synaptic and intratumoural TM-connectivity. Arrows denote presynaptic VGLUT1 clusters (blue); arrowheads denote GluR1 clusters (red) located on crossing, connected TMs (green). **k**, Electron microscopy images of a PDX S24 glioma cell showing 2 NGS (top right and bottom right) in the vicinity of a TM crossing (top left) (7 observations in $n = 3$ experiments). **l**, Quantification of relative SR101 signal intensity in single glioma cells ($n = 116$ TM connected versus $n = 36$ TM unconnected cells in 3 S24 PDX mice). *P* value determined by two-sided Mann–Whitney test **m**, Single-cell gene expression analysis of a human IDH-mutated astrocytoma showing a distinct gene expression pattern in cell clusters positive for ApoE. **n**, Connectivity score of single tumour cells (see Supplementary Methods) is significantly correlated with ApoE cluster assignment ($n = 1{,}911$ single cells from 4 patients with IDH mutated astrocytomas). *P* value determined by two-sided Mann–Whitney test. **o**, *GRIA1* expression of single tumour cells in the ApoE-negative versus ApoE-positive cluster ($n = 1{,}911$ single cells from 4 patients with IDH mutated astrocytomas). *P* value determined by two-sided Mann–Whitney test. **p**, **q**, Gene Ontology (GO) term analysis of representative ApoE-positive clusters from patients with IDH-mutated astrocytoma (**p**) and GB (**q**) associated with neuronal and synapse-associated processes (top 15 GO terms shown). All associated GO terms of all ApoE-positive clusters as well as ApoE-negative clusters can be found in Supplementary Tables 5 and 6. The false discovery rate was kept below 0.05. *P* values determined by Fisher's exact test. For sample size, see 'Statistics and reproducibility' in Supplementary Methods. Data are mean ± s.e.m.

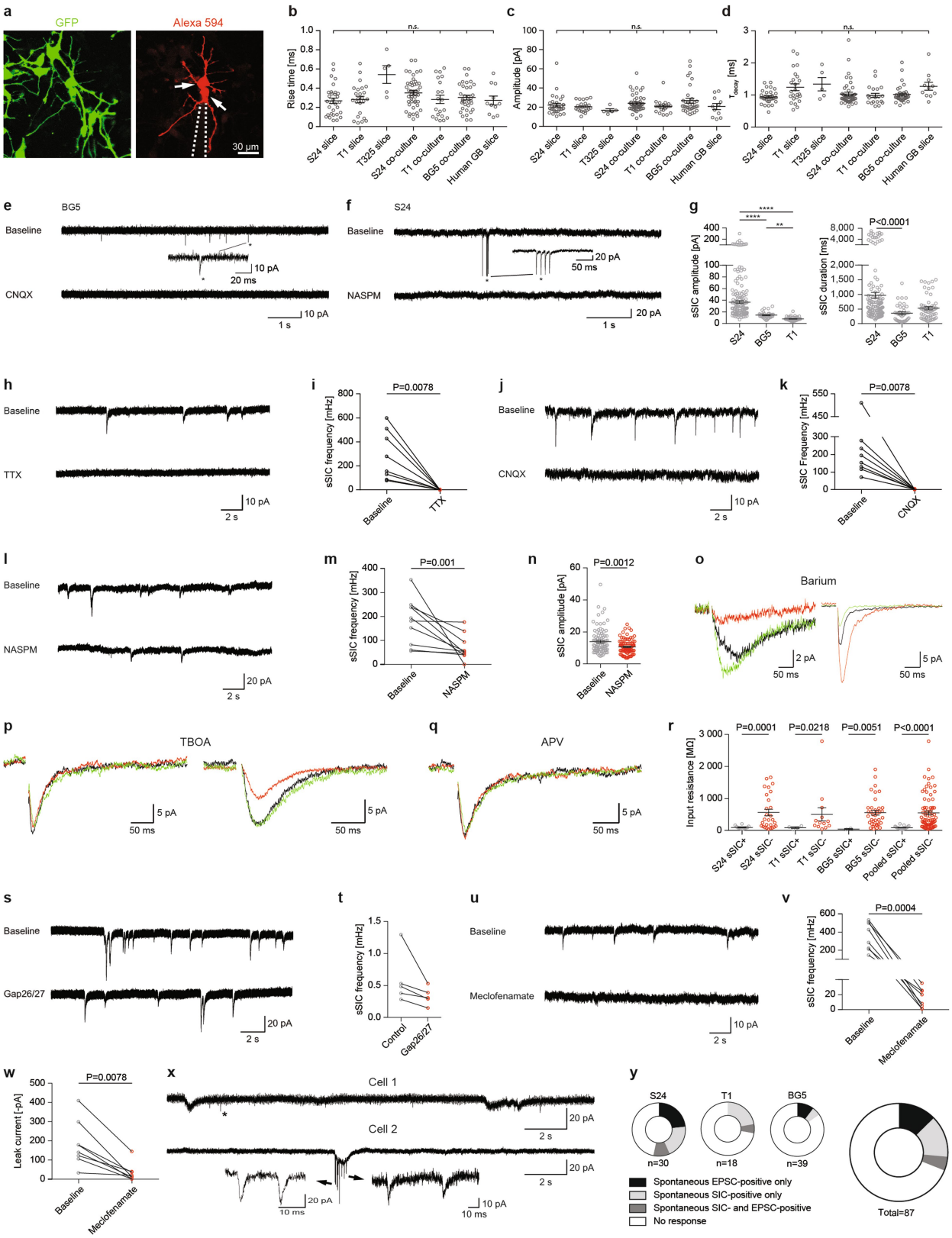

Extended Data Fig. 5 | See next page for caption.

Extended Data Fig. 5 | Electrophysiological characterization of EPSCs and SICs in glioma cells. a, Representative glioma cells expressing GFP (green) filled with Alexa 594 via the patch pipette (red, one example of $n = 720$ filled cells). Note that only the bottom of the two cells marked with arrows was recorded in whole-cell configuration. The top glioma cell was presumably filled via gap junctions. **b**–**d**, Quantitative properties of EPSCs in different glioma models resemble normal AMPAR kinetics ($n = 171$ EPSCs in 7 different models; Supplementary Methods for details). n.s., not significant; two-sided Kruskal–Wallis test with post hoc Dunn's multiple comparisons test. **e**, Representative traces showing inhibition of spontaneous EPSCs by CNQX in BG5 co-culture. **f**, Representative traces of spontaneous EPSC inhibition with NASPM in S24 co-culture ($n = 2$ cells). **g**, Quantification of spontaneous SIC amplitude and duration across different cell lines (S24 $n = 203$ SICs, BG5 $n = 39$ SICs, T1 $n = 55$ SICs). $^{**}P < 0.01$, $^{****}P < 0.0001$, two-sided Kruskal–Wallis test with post hoc Dunn's multiple comparisons test. **h**, **i**, Representative traces of spontaneous SIC inhibition with TTX in S24 co-culture (**h**) and corresponding quantification (**i**) ($n = 8$ cells). *P* value determined by two-sided Wilcoxon matched pairs test. **j**, **k**, Representative traces of spontaneous SIC inhibition with CNQX in S24 co-culture (**j**) and corresponding quantification (**k**) ($n = 8$ cells). *P* value determined by two-sided Wilcoxon matched pairs test. **l**, **m**, Representative traces of spontaneous SIC inhibition with NASPM in S24 co-culture (**l**) and corresponding quantification (**m**) ($n = 10$ cells). *P* value determined by two-sided paired *t*-test. **n**, Quantification of spontaneous SIC amplitude in baseline compared to NASPM ($n = 100$ spontaneous SICs baseline versus $n = 98$ spontaneous SICs under NASPM). *P* value determined by two-sided Mann–Whitney test. **o**–**q**, Pharmacological characterization of evoked SICs in S24 co-culture. Note the differing effects of TBOA and barium on individual cells (black denotes baseline; red denotes drug; green denotes washout). **r**, Quantification of access resistance in different cell lines, grouped by spontaneous slow inward current positivity. In all cell lines, sSIC-positive ($sSIC^+$) cells show significantly lower access resistance (two-sided unpaired *t*-test with Welch's correction, S24 $n = 12$ $sSIC^+$ cells versus $n = 28$ $sSIC^-$ cells; two-sided Mann–Whitney test, T1 $n = 4$ $sSIC^+$ cells versus $n = 13$ $sSIC^-$ cells, BG5 $n = 2$ $sSIC^+$ cells versus $n = 38$ $sSIC^-$ cells, pooled $n = 18$ $sSIC^+$ cells versus $n = 79$ $sSIC^-$ cells). **s**, **t**, Representative traces (**s**) and corresponding quantification (**t**) showing inhibition of sSIC frequency with GAP26 and GAP27 in S24 co-culture ($n = 5$ cells). **u**, **v**, Representative traces (**u**) and corresponding quantification (**v**) showing inhibition of spontaneous spontaneous SICs by meclofenamate ($n = 8$ cells). *P* value determined by two-sided paired *t*-test. **w**, Quantification, showing meclofenamate significantly decreases the leak current of tumour cells (two-sided Wilcoxon matched-pairs signed rank test, $n = 8$ cells). **x**, Example traces from two different cells showing that spontaneous SICs and sEPSCs can occur simultaneously or separately. EPSCs are marked by asterisks in the top trace. Magnification of EPSCs occurring on top of slow inward currents is shown in the bottom trace and marked by arrows. **y**, Quantification of different electrophysiological subgroups of glioma cells in different cell lines (S24 $n = 30$ cells, T1 $n = 18$ cells, BG5 $n = 39$ cells) and summary of electrophysiological subgroups across different glioma cell lines in co-culture. Data are mean ± s.e.m.

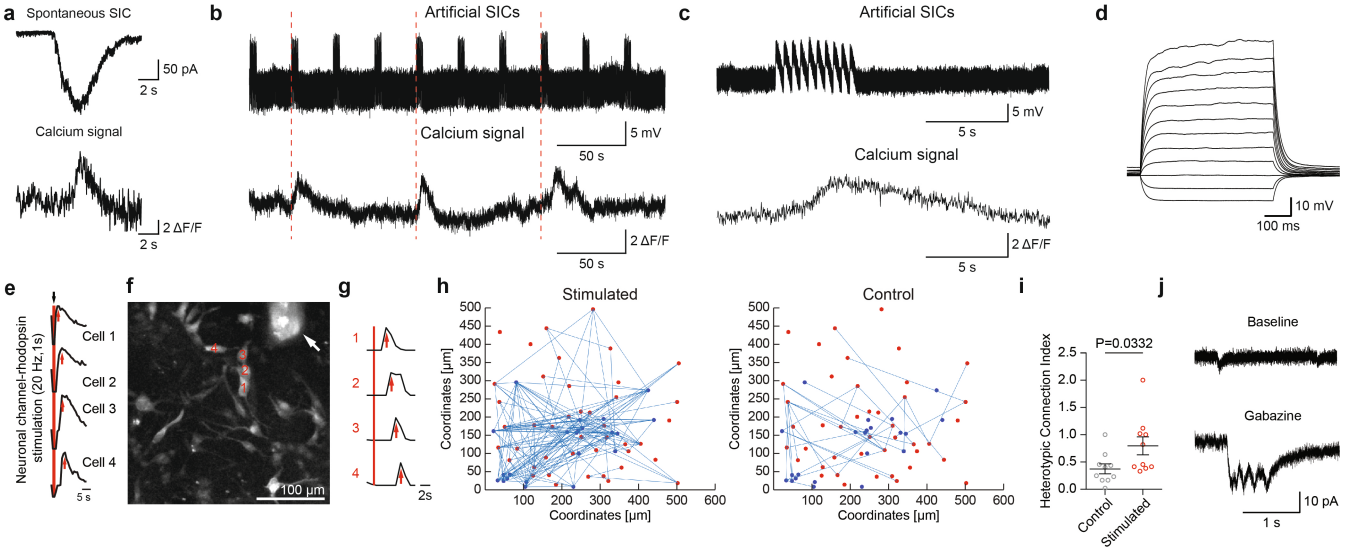

Extended Data Fig. 6 | Neuronal input triggers glioma network activation. a, Spontaneous SIC with temporally correlated calcium transient in high magnification. **b**, **c**, Representative traces of voltage response to current injection simulating slow inward currents (top) and simultaneous calcium trace (bottom) in two different time scales. **d**, Representative current-clamp recording from a PDX S24 glioma cell selected from a total of $n = 318$ recordings from different models. Voltage responses to current injections (−80 to 360 pA; step size, 40 pA). **e**, Individual glioma cells of one tumour microregion respond to ChR2 stimulation with different latencies. Calcium traces of individual glioma cells were normalized to values between 0 and 1. **f**, Standard deviation projection of calcium time-series imaging of GCaMP6 fluorescence in S24 cells co-cultured with neurons. Arrow denotes bipolar stimulation electrode; numbers 1 to 4 correspond to individual tumour cells in **g**. **g**, Different latencies of calcium responses to neuronal stimulation. **h**, Representative coactivity maps of functionally neuron-connected glioma cells (blue) and non-neuron connected glioma cells (red) after neuronal ChR2 stimulation. **i**, Quantification of connections between functionally neuron-connected glioma cells and non-neuron connected glioma cells before and after neuronal ChR2 stimulation, normalized to the number of functionally neuron-connected glioma cells ($n = 10$ experiments in 5 S24 PDX mice, see Supplementary Methods). *P* value determined by two-sided Mann–Whitney test. **j**, Representative traces showing gabazine-induced stacking of slow currents into prolonged events ($n = 8$ cells in S24 co-culture). Data are mean ± s.e.m.

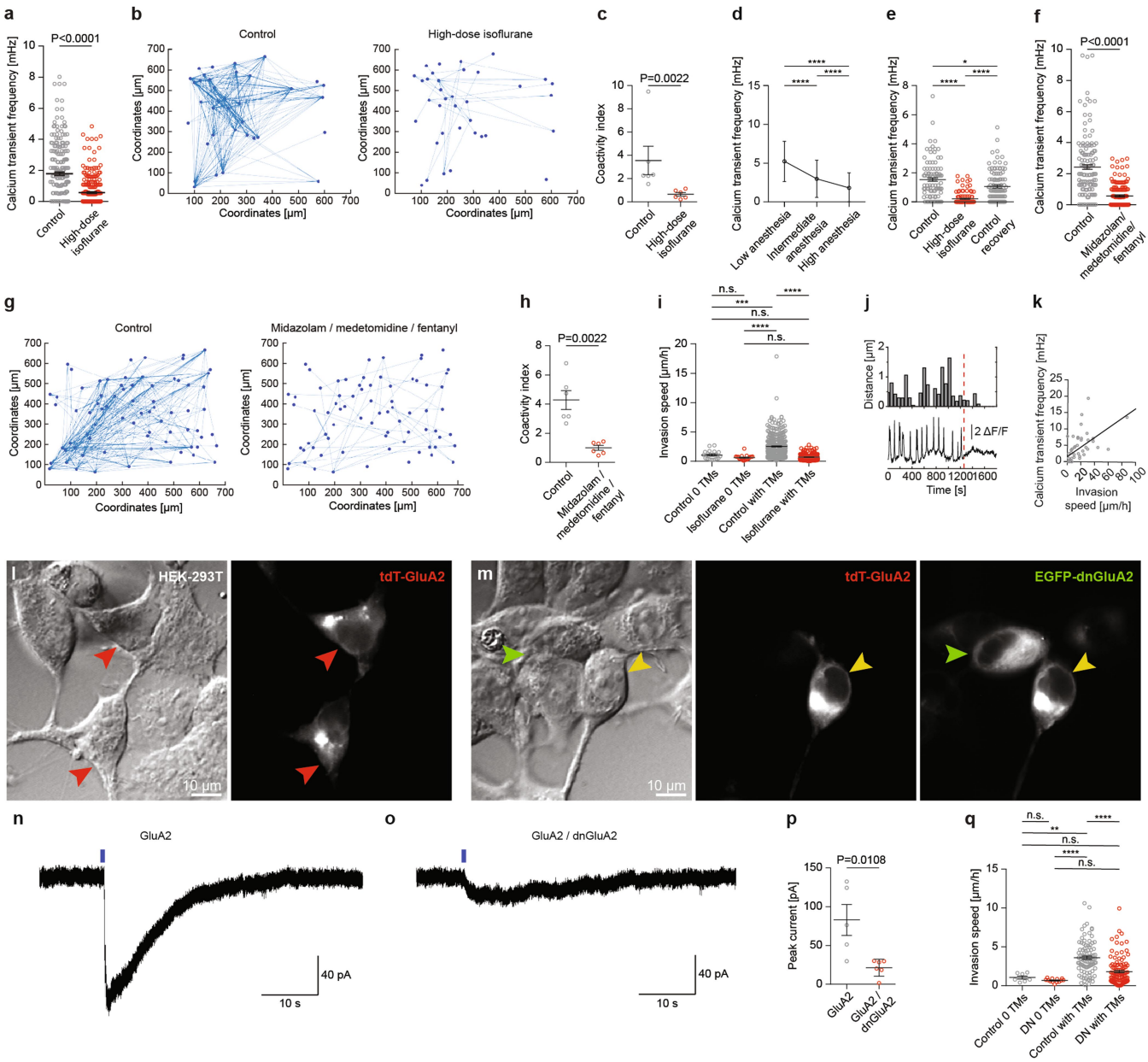

Extended Data Fig. 7 | See next page for caption.

Extended Data Fig. 7 | General anaesthesia silences glioma networks and effects of neuron-induced calcium transients on invasion speed. **a**, In vivo calcium transient frequency under control conditions and deep anaesthesia. Calcium transient frequency of S24 PDX glioma cells imaged during deep anaesthesia with isoflurane compared with control (minimal dose anaesthesia) conditions ($n = 274$ cells per group in 3 S24 PDX mice). *P* value determined by two-sided Mann–Whitney test. **b**, Representative coactivity maps of glioma cells under control conditions versus deep anaesthesia. **c**, Calcium transient coactivity indices under both conditions ($n = 6$ experiments in 3 mice). *P* value determined by two-sided Mann–Whitney test. **d**, Three-step anaesthesia experiment of calcium transient frequency during different stages of isoflurane anaesthesia ($n = 160$ cells per group; in 3 S24 PDX mice. Data are s.d.). $^{****}P < 0.0001$, two-sided Kruskal–Wallis test with post hoc Dunn's multiple comparisons test. **e**, Calcium transient frequency before, during and after isoflurane anaesthesia ($n = 106$ cells per group; in 2 S24 PDX mice). $^{*}P < 0.05$; $^{****}P < 0.0001$, two-sided Kruskal–Wallis test with post hoc Dunn's multiple comparisons test. **f**, In vivo calcium transient frequency under control conditions and deep anaesthesia. Calcium transient frequency from S24 PDX glioma cells imaged during deep anaesthesia with a mixture of midazolam, medetomidine and fentanyl compared with control (minimal dose anaesthesia) conditions ($n = 154$ cells per group in 3 S24 PDX mice). *P* value determined by two-sided Mann–Whitney test. **g**, Representative coactivity maps of glioma cells under control conditions versus deep anaesthesia. **h**, Calcium transient coactivity indices under both conditions ($n = 6$ experiments in 3 mice). *P* value determined by two-sided Mann–Whitney test. **i**, Quantification of invasion speeds of glioma cells in vivo under control conditions versus isoflurane anaesthesia with respect to glioma cells possessing TMs (control: $n = 21$ cells without TMs in 4 mice and $n = 234$ cells with TMs in 3 mice, isoflurane anaesthesia: $n = 16$ cells without TMs in 3 mice and $n = 127$ cells with TMs in 3 mice). $^{***}P < 0.001$, $^{****}P < 0.0001$, two-sided Kruskal–Wallis test with post hoc Dunn's multiple comparisons test. **j**, Temporal correlation between individual calcium fluctuations (bottom trace) of Rhod2-AM-loaded glioma cells and individual cell movement during migration. Note that the cessation of calcium transients (marked by the dashed red line) correlated with a decrease in cell mobility. **k**, Relationship between the frequency of calcium transients and the migration speed of glioma cells ($n = 51$ cells in S24 co-culture). $P < 0.0001$, two-sided linear regression; Pearson correlation coefficient is 0.57, r^2 value is 0.327. **l**, Differential interference contrast (DIC) (left) and fluorescent (right) images of HEK-293T cells transfected with a tdTomato-GluA2 (tdT-GluA2) plasmid. Cells expressing tdT-GluA2 are indicated by red arrowheads. **m**, DIC (left) and fluorescent (middle and right) images of HEK-293T cells transfected with tdTomato-GluA2 and DN-GluA2-GFP plasmids. Cells expressing eGFP-dnGluA2 or both eGFP-dnGluA2 and tdTomato are indicated by green or yellow arrowheads, respectively. **n**, **o**, Example trace showing GluA2 homotetramer-mediated currents, in whole-cell voltage clamp mode, in response to uncaged glutamate (blue box) on cells expressing GluA2 (**n**) and both GluA2 and dnGluA2 (**o**). **p**, Peak current in GluA2 cells and in cells expressing both GluA2 and DN-GluA2 subunits ($n = 5$ GluA2 cells and $n = 6$ GluA2/dnGluA2 cells). *P* value determined by two-sided Mann–Whitney test. Data are mean ± s.e.m. **q**, Quantification of invasion speed of DN-GluA2-GFP and tdTomato cells compared with control cells with respect to glioma cells possessing TMs (control without TMs $n = 7$ cells, control with TMs $n = 94$ cells; DN without TMs $n = 15$ cells, DN with TMs $n = 114$ cells in 5 mice). $^{**}P < 0.01$, $^{****}P < 0.0001$, two-sided Kruskal–Wallis test with post hoc Dunn's multiple comparisons test. Data are mean ± s.e.m.

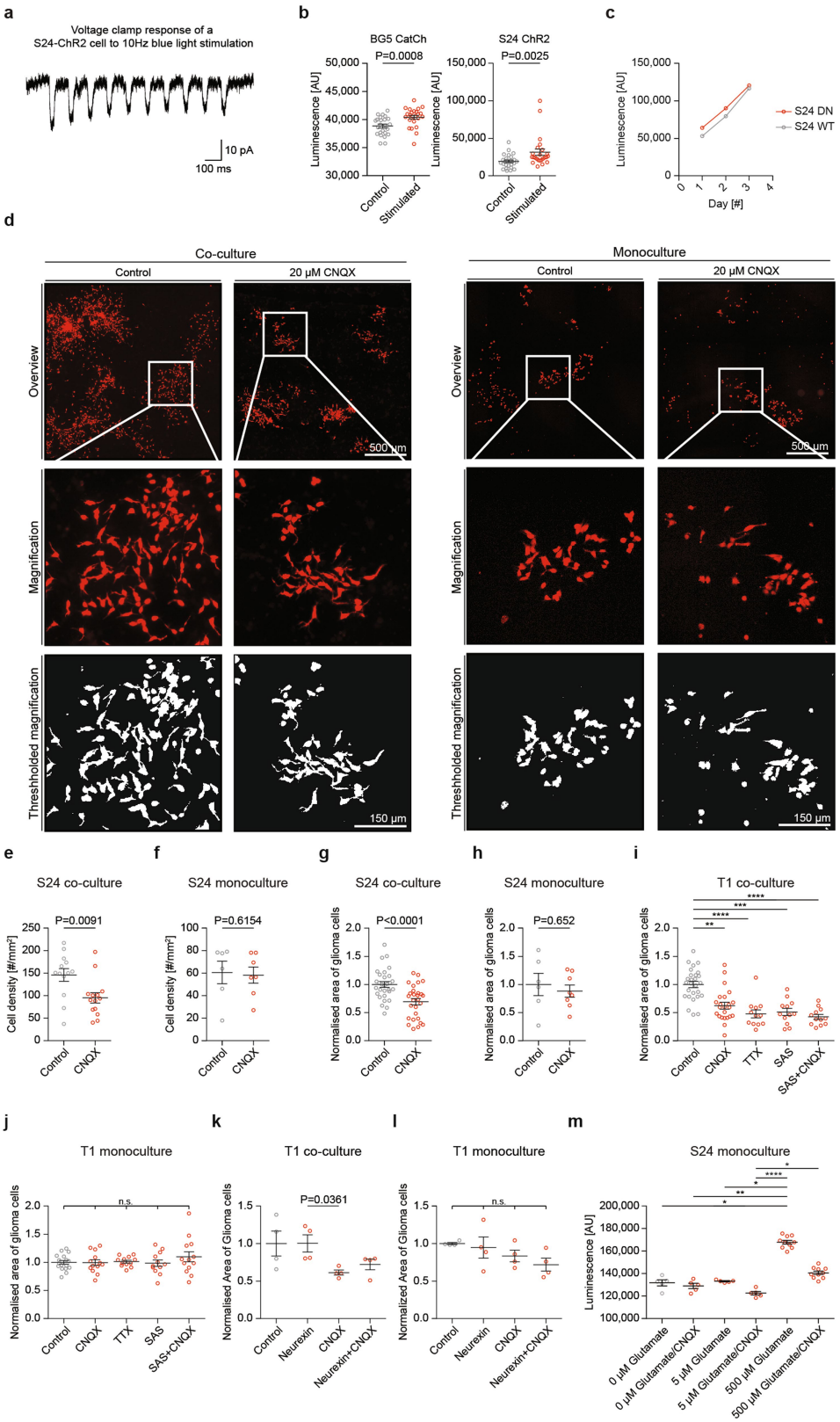

Extended Data Fig. 8 | See next page for caption.

Extended Data Fig. 8 | Validation of functional NGS effects in vitro. **a**, Demonstration of depolarizing inward current in S24 ChR2 cells in response to 10-Hz pulses of blue light as measured in voltage clamp. **b**, Comparison of proliferation with the CellTiter-Glo assay after three days of stimulation (BG5 calcium-translocating channelrhodopsin (CatCh) and S24 ChR2 glioblastoma cells) in monocultures (BG5 CatCh $n = 24$ samples per group; S24 ChR2 $n = 24$ samples per group). *P* values determined by two-sided Mann–Whitney test. **c**, In vitro growth analysis of GluA2-DN-GFP and tdTomato S24 glioma cells (DN) and control cells (WT) in monoculture reveal no significant difference in proliferation rate between cell lines ($n = 16$ technical replicates for each group and day, one representative experiment out of three, two-sided Mann-Whitney test). **d**, Representative epifluorescence images of S24 glioma cells co-cultured with neurons (left) or cultured alone (right). The area marked in the top panel is shown magnified in the central panels. Thresholded images are used for automated quantification (bottom; see Supplementary Methods). **e**, **g**, Co-cultures of S24 glioma cells and neurons treated with the AMPAR antagonist 20 μM CNQX for 8 days grow more slowly and therefore show lower glioma cell densities (**e**) and smaller areas covered by glioma cells (**g**) than controls (**e**, $n = 13$ coverslips control and $n = 14$ coverslips CNQX; **g**, $n = 30$ coverslips control and $n = 28$ coverslips CNQX). **f**, **h**, Monocultures of S24 glioma cells generally grow more slowly than co-cultures, but show no significant effect of treatment with 20 μM CNQX on cell densities (**f**) or area covered by glioma cells (**h**) (**f**, $n = 6$ coverslips control and $n = 7$ coverslips CNQX; **h**, $n = 6$ coverslips control and $n = 8$ coverslips CNQX). **i**, **j**, Quantification of relative T1 glioma cell area in co-culture with neurons (**i**) and in monoculture (**j**), after 8 days of treatment with CNQX, TTX, SAS or SAS plus CNQX, leading to a significant decrease in the proliferation of T1 tumour cells cultured with neurons while not significantly affecting cells in monoculture (**i**, control: $n = 27$ coverslips, CNQX: $n = 23$ coverslips, TTX, SAS, SAS + CNQX: $n = 12$ coverslips, two-sided Kruskal-Wallis test, post hoc Dunn's multiple comparisons test; **j**, control: $n = 17$ coverslips, CNQX, SAS + CNQX: $n = 13$ coverslips, TTX, SAS: $n = 12$ coverslips, two-sided ordinary one-way ANOVA, post hoc Holm–Sidak's multiple comparisons test). **k**, **l**, Quantification of relative T1 glioma cell area in co-culture with neurons (**k**) and in monoculture (**l**) after 8 days of treatment with neurexin 1β, CNQX or both neurexin 1β and CNQX ($n = 4$ coverslips for each group). Only CNQX treatment leads to a significant decrease in proliferation of T1 co-cultured tumour cells. **m**, The effects of different concentrations of glutamate on cell proliferation were tested in monocultures of S24 glioma cells. The pro-proliferative effect of glutamate can be partially abrogated by CNQX ($n = 10$ for 500 μM glutamate and 500 μM glutamate/CNQX; $n = 5$ for all other groups). See Supplementary Methods for further details. *P* values determined by two-sided unpaired *t*-test (**e**, **g**, **h**), two-sided Mann–Whitney test (**f**), two-sided Kruskal–Wallis test, post hoc Dunn's multiple comparisons test (**i**, **k**–**m**), or two-sided ordinary one-way ANOVA, post hoc Holm-Sidak's multiple comparisons test (**j**). Data are mean ± s.e.m.

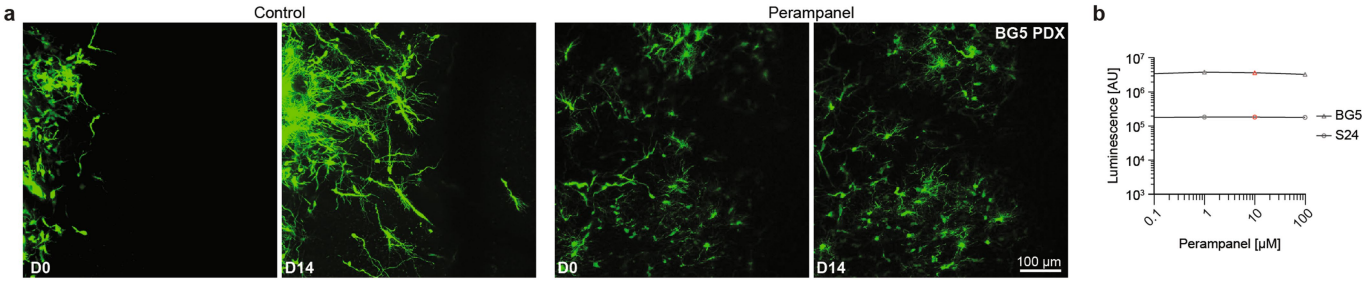

Extended Data Fig. 9 | Inhibition of glioma growth by perturbation of AMPAR signalling. a, BG5 PDX glioma regions imaged in vivo on days 0 and 14 under control conditions and after treatment with AMPAR antagonist perampanel ($n = 25$ control and $n = 29$ perampanel FOVs in 5 (control) and 6 (perampanel) mice; see Fig. 5k). **b**, Cell viability of S24 and BG5 glioma cells exposed to different concentrations of perampanel (1–100 µM) in monocultures in vitro ($n \geq 3$ wells per condition, 2 biological independent experiments).

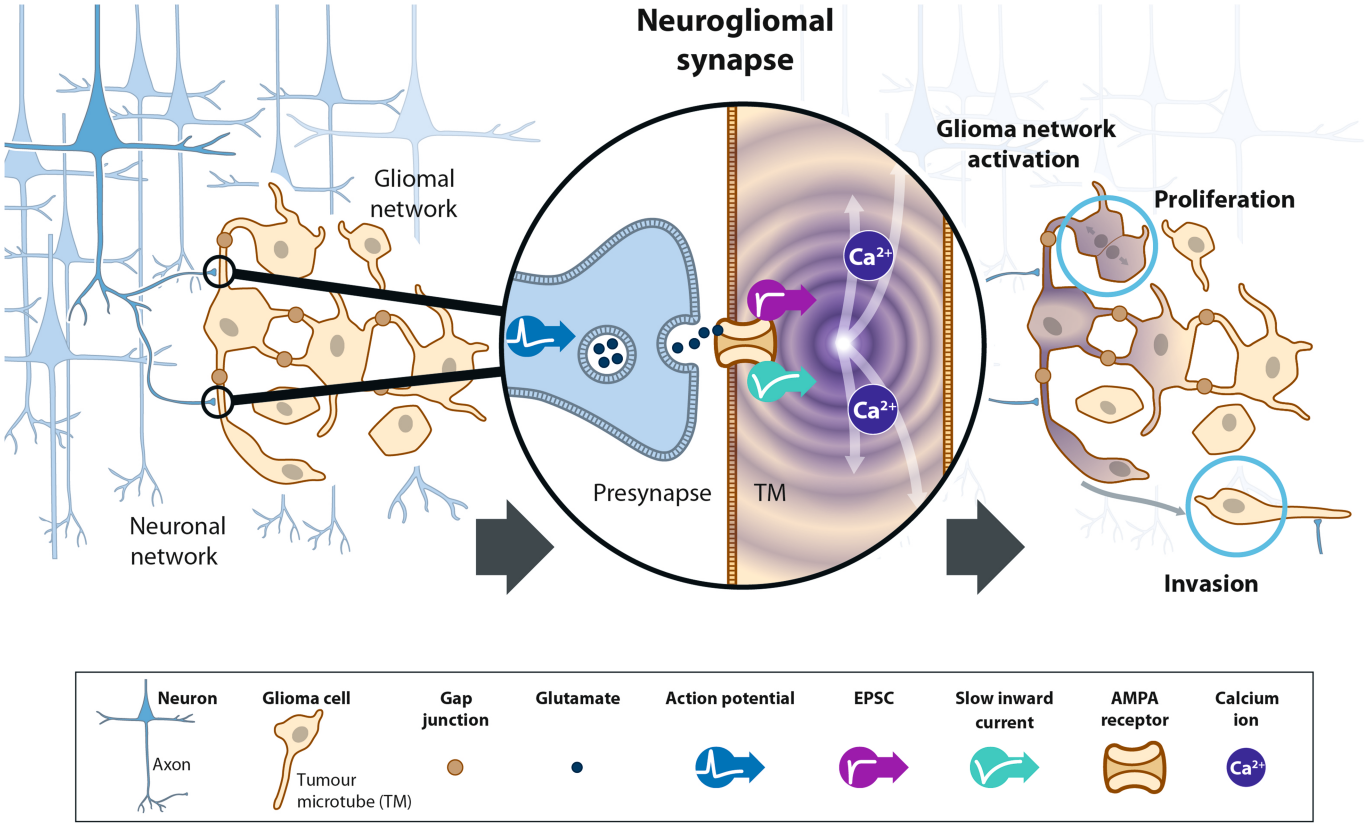

Extended Data Fig. 10 | Schematic illustration of neurogliomal synapses and their functional role in brain tumour progression. The left of the scheme illustrates the neuronal network, the glioma network, and their interconnectivity. A magnified scheme of a neurogliomal synapse is shown in the centre. The consequence of NGS function for brain tumour biology is illustrated on the right.

Corresponding author(s): Frank Winkler, Varun Venkataramani, Thomas Kuner

Reporting Summary

Nature Research wishes to improve the reproducibility of the work that we publish. This form provides structure for consistency and transparency in reporting. For further information on Nature Research policies, see Authors & Referees and the Editorial Policy Checklist.

Statistical parameters

When statistical analyses are reported, confirm that the following items are present in the relevant location (e.g. figure legend, table legend, main text, or Methods section).

n/a	Confirmed
☐	☒ The exact sample size (*n*) for each experimental group/condition, given as a discrete number and unit of measurement
☐	☒ An indication of whether measurements were taken from distinct samples or whether the same sample was measured repeatedly
☐	☒ The statistical test(s) used AND whether they are one- or two-sided *Only common tests should be described solely by name; describe more complex techniques in the Methods section.*
☐	☒ A description of all covariates tested
☐	☒ A description of any assumptions or corrections, such as tests of normality and adjustment for multiple comparisons
☐	☒ A full description of the statistics including central tendency (e.g. means) or other basic estimates (e.g. regression coefficient) AND variation (e.g. standard deviation) or associated estimates of uncertainty (e.g. confidence intervals)
☐	☒ For null hypothesis testing, the test statistic (e.g. *F*, *t*, *r*) with confidence intervals, effect sizes, degrees of freedom and *P* value noted *Give P values as exact values whenever suitable.*
☒	☐ For Bayesian analysis, information on the choice of priors and Markov chain Monte Carlo settings
☒	☐ For hierarchical and complex designs, identification of the appropriate level for tests and full reporting of outcomes
☐	☒ Estimates of effect sizes (e.g. Cohen's *d*, Pearson's *r*), indicating how they were calculated
☐	☒ Clearly defined error bars *State explicitly what error bars represent (e.g. SD, SE, CI)*

Our web collection on statistics for biologists may be useful.

Software and code

Policy information about availability of computer code

Data collection	Scanning electron microscopy data were acquired using the ATLAS software system 5.2.0.63. Electron tomography data were acquired with the SerialEM software (Version 3.4). In-vivo MPLSM data were acquired using either ZEN Version 14.0.18.201 (Zeiss) or ImSpector Version 5.1.325 (LaVision) software. Blue light stimulation in in in-vivo imaging experimental paradigms was triggered with a custom-written MATLAB script (MATLAB version R2016a (9.0.0.341360)) . Blue light stimulation in-vitro for electrophysiology experiments was triggered via the PatchMaster software v2x90.3. Blue light stimulation in-vitro for cell proliferation experiments was triggered via a custom-written script in the Arduino language. dSTORM microscopy data were acquired using a custom-written software in Java. Data was collected with FACS Diva Software (version 9, BD Biosciences). FACS analyses were performed with FlowJo Version 10.5.x. Electrophysiology data were acquired using PatchMaster v2x90.3. Confocal data were acquired using the LAS software Version 2.7.3.9723 on a Leica SP5 setup and LAS software version 3.5.2.18963 on a Leica SP8 setup. RNA sequencing was performed with the commercial software of the HiSeq2000 v4 machine (Illumina, HCS 2.2.58). The filtered reads were mapped with STAR 2.3 against human genome 38 and PicardTools 1.78 with CollectRNASeqMetrics were used for quality checking. Count data were generated by htseq-count using the gencode.v26.annotation.gtf file for annotation. DESeq2 1.4.1 was run with default parameters for the groups comparison.
Data analysis	For all imaging data Fiji (Image J 1.51N, 1.52A) was used for analysis. Electron microscopy data were analysed with the IMOD software suite which included 3Dmod for 3D reconstruction (Version 4.9.5), the TrakEM Fiji Plugin and Fiji (Image J 1.51N, 1.52A) . For electrophysiology analysis Igor Pro 6.2.1.0, PatchMaster v2x90.3 and MATLAB R2016b were used. Single cell expression data was reanalyzed using customized scripts in R (www.r-project.org, 1012 version 3.5.1) based on the open source packages "seurat" (version 2.3.4) and "scater" (version 3.7). MATLAB R2016b(9.1.0.441655) was used for custom-written scripts for the calcium imaging and invasion analysis. For statisical analysis GraphPad Prism v.5.02 and GraphPad Prism v.6.01 were used. Cell Profiler Version 3.1.5 was used

for semi-automatic cell counting. Imaris 6.3 was used for three-dimensional visualization of imaging data. PANTHER 14.1 was used for gene ontology analysis.

For manuscripts utilizing custom algorithms or software that are central to the research but not yet described in published literature, software must be made available to editors/reviewers upon request. We strongly encourage code deposition in a community repository (e.g. GitHub). See the Nature Research guidelines for submitting code & software for further information.

Data

Policy information about availability of data

All manuscripts must include a data availability statement. This statement should provide the following information, where applicable:

- Accession codes, unique identifiers, or web links for publicly available datasets
- A list of figures that have associated raw data
- A description of any restrictions on data availability

Bulk RNA-Seq data have been deposited in the SRA database under the accession number PRJNA554870. Single-cell RNA sequencing data can be accessed under the GEO accession numbers GSE84465 and GSE89567. Clinical data of patient samples can be found in the Supplementary Table 2. All other data and code that support the findings of this study are available from the corresponding authors on reasonable request. All source data for every figure are included in the supporting information that accompanies the paper.

Field-specific reporting

Please select the best fit for your research. If you are not sure, read the appropriate sections before making your selection.

☒ Life sciences ☐ Behavioural & social sciences ☐ Ecological, evolutionary & environmental sciences

For a reference copy of the document with all sections, see nature.com/authors/policies/ReportingSummary-flat.pdf

Life sciences study design

All studies must disclose on these points even when the disclosure is negative.

Sample size	Samples sizes from other experiments were estimated from similar experiments in former publications of the group.
Data exclusions	The bootstrap analysis to classify cells into responsive and non-responsive to neuronal channel-rhodopsin used a 95 percentile cutoff for each pixel as predefined criterion. For invasion analysis of cells upon neuronal channel-rhodopsin analysis and cells with spontaneous calcium transients cells with 1-2 TMs were selected as predefined criterion as they have been previously described as predominant population showing migratory behaviour. No relevant other data was excluded from analysis.
Replication	All experiments and measures taken are reproducible and all observations across models were made at least twice. Reproducibility of human sample data is depending on sample availability.
Randomization	Mice of matched age and samples were randomly allocated to the experiments.
Blinding	Collection of animal samples was not blinded. However, samples were analyzed blinded afterwards.

Reporting for specific materials, systems and methods

Materials & experimental systems

n/a	Involved in the study
☐	☒ Unique biological materials
☐	☒ Antibodies
☐	☒ Eukaryotic cell lines
☒	☐ Palaeontology
☐	☒ Animals and other organisms
☐	☒ Human research participants

Methods

n/a	Involved in the study
☒	☐ ChIP-seq
☐	☒ Flow cytometry
☐	☒ MRI-based neuroimaging

Unique biological materials

Policy information about availability of materials

Obtaining unique materials	Reproducibility of human sample data is depending on sample availability. All other unique materials used are readily available from the authors.

Antibodies

Antibodies used	The following primary antibodies were used: EGFRvIII[clone L8A4] splice variant-specific antibody (absolute antibody; Ab00184; mouse; Lot T1514B05; 1:50,); GFP (Abcam; ab13970, polyclonal; chicken; Lot GR236651-16, GR279236; 1:500), GFP (Abcam; ab6556; polyclonal; Lot 313896-2; rabbit; 1:500), Homer 1/2/3 (Synaptic System; 160103; rabbit; polyclonal; Lot 160103/5, 160 103/4, 160103/1-7; 1:200), IDH1-R132H (Dianova; clone DIA H09; mouse; Lot 161221/03; Lot 1637/03, 181011/96, 181011/93; 1:2), Nestin (Abcam; ab105389; clone [SP103]; rabbit; Lot GR295268-2, GR281699-1, GR198440-6, GR261050-1; 1:100), Nestin (Abcam; ab22035; clone [10C2] , mouse; Lot GR303487-1, GR207026, GR312885-4, GR324070755; 1:100), Nestin (Abcam; ab6320; mouse; clone [196908]; Lot GR290003-1, GR188432-1; GR252900-1; 1:100), Nestin (Millipore; MAB5326; mouse; Lot 2697590; 1:200), vGluT1 (Millipore; AB5905; polyclonal; guinea pig; Lot 3193844, 2647529; 1:500), turboGFP (Origene, TA150041; clone OTI2H8 (formerly 2H8); Lot 51301010812, 5M19-W004-1.00; mouse; 1:100).
Validation	EGFRvIII[L8A4] splice variant-specific antibody (absolute antibody; Ab00184; mouse; 1:50): Wikstrand CJ, Hale LP, Batra SK, Hill ML, Humphrey PA, Kurpad SN, McLendon RE, Moscatello D, Pegram CN, Reist CJ, et al., Monoclonal antibodies against EGFRvIII are tumor specific and react with breast and lung carcinomas and malignant gliomas., Cancer Res. 1995 Jul 15;55(14):3140-8. Validation statement on manufacturer's website. GFP (Abcam; ab13970; chicken; 1:500): Handara G, Hetsch FJA, Jüttner R, Schick A, Haupt C, Rathjen FG, Kröger S. The role of agrin, Lrp4 and MuSK during dendritic arborization and synaptogenesis in cultured embryonic CNS neurons. Dev Biol. 2019 Jan 1;445(1):54-67. doi: 10.1016/j.ydbio.2018.10.017. Epub 2018 Oct 29. Validated in WB, IHC, ICC/IF by the provider GFP (Abcam; ab6556; rabbit; 1:500): Palmer WH et al. Induction and Suppression of NF-?B Signalling by a DNA Virus of Drosophila. J Virol 93:N/A (2019). Validated in IHC-FoFr, Electron Microscopy, IHC-P, IHC-Fr, IP, WB, ICC/IF, Flow Cytometry by the provider. Homer 1/2/3 (Synaptic System; 160103; rabbit; 1:200): Crosby ND, Zaucke F, Kras JV, Dong L, Luo ZD, Winkelstein BA. Homer is concentrated at the postsynaptic density and does not redistribute after acute synaptic stimulation. Neuroscience. 2014 Apr 25;266:80-90. doi: 10.1016/j.neuroscience.2014.01.066. Epub 2014 Feb 12. IDH1-R132H (Dianova; DIA H09; mouse; 1:2): Capper D, Zentgraf H, Balss J, Hartmann C, von Deimling A. Monoclonal antibody specific for IDH1 R132H mutation. Acta Neuropathol. 2009 Nov;118(5):599-601. doi: 10.1007/s00401-009-0595-z. Epub 2009 Oct 2. Nestin (Abcam; ab105389; rabbit; 1:100): Malchenko S, Sredni ST, Boyineni J, Bi Y, Margaryan NV, Guda MR, Kostenko Y, Tomita T, Davuluri RV, Velpula K, Hendrix MJC, Soares MB. Characterization of brain tumor initiating cells isolated from an animal model of CNS primitive neuroectodermal tumors. Oncotarget. 2018 Feb 9;9(17):13733-13747. doi: 10.18632/oncotarget.24460. eCollection 2018 Mar 2. Knock-out validated by provider. Nestin (Abcam; ab22035; mouse; 1:100): Gudbergsson JM, Kostrikov S, Johnsen KB, Fliedner FP, Stolberg CB, Humle N, Hansen AE, Kristensen BW, Christiansen G, Kjær A, Andresen TL, Duroux M. A tumorsphere model of glioblastoma multiforme with intratumoral heterogeneity for quantitative analysis of cellular migration and drug response. Exp Cell Res. 2019 Jun 1;379(1):73-82. doi: 10.1016/j.yexcr.2019.03.031. Epub 2019 Mar 25. Nestin (Millipore; MAB5326; mouse; 1:200): Lee CW, Zhan Q, Lezcano C, Frank MH, Huang J, Larson AR, Lin JY, Wan MT, Lin PI, Ma J, Kleffel S, Schatton T, Lian CG, Murphy GF. Nestin depletion induces melanoma matrix metalloproteinases and invasion. Lab Invest. 2014 Dec;94(12):1382-95. doi: 10.1038/labinvest.2014.130. Epub 2014 Nov 3. Validated for use in IC, IH, IH(P), WB by the provider. vGluT1 (Millipore; AB5905; guinea pig; 1:500): Buren C, Tu G, Parsons MP, Sepers MD, Raymond LA. Influence of cortical synaptic input on striatal neuronal dendritic arborization and sensitivity to excitotoxicity in corticostriatal coculture. J Neurophysiol. 2016 Aug 1;116(2):380-90. doi: 10.1152/jn.00933.2015. Epub 2016 Apr 27. Validated for use in immunohistochemistry for the detection of Vesicular Glutamate Transporter 1 by the provider. turboGFP (Origene, TA150041; mouse, 1:100): Rodriguez-Terrones D, Gaume X, Ishiuchi T, Weiss A, Kopp A, Kruse K, Penning A, Vaquerizas JM, Brino L, Torres-Padilla ME. A molecular roadmap for the emergence of early-embryonic-like cells in culture. Nat Genet. 2018 Jan;50(1):106-119. doi: 10.1038/s41588-017-0016-5. Epub 2017 Dec 18.

Eukaryotic cell lines

Policy information about cell lines

Cell line source(s)	Patient-derived xenograft models (S24, T1, T325, T269, BG5, E2, IOMM, TS603).
Authentication	Authentication of GBSCs with Illumina Infinium Methylation Analysis in August 2018 with >850,000 CpG sites. TS603 was molecularly revalidated for the IDHR132H mutation and 1p/19q co-deletion. The meningioma cell line was regularly checked via genome fingerprinting.
Mycoplasma contamination	Cell lines were tested negative for mycoplasma contamination.
Commonly misidentified lines (See ICLAC register)	No commonly misidentified cell line was used.

Animals and other organisms

Policy information about studies involving animals; ARRIVE guidelines recommended for reporting animal research

Laboratory animals	Mice were maintained in a specific-pathogen-free environment according to the University Hospital of Heidelberg guidelines and fed with a standard diet. Immunodeficient nude mice NMRI were purchased from Charles River. NSG (NOD scid gamma) mice were bred at the DKFZ animal facility. 8-12 week old NMRI nude mice and NSG (NOD scid gamma) were used. Nestin-Tv-a;Tlx-GFP mice (5.5-6.5 weeks) in combination with RCAS-PDGFB/AKT vectors were provided by Haikun Liu. Only male mice were used.
Wild animals	The study did not involve wild animals.
Field-collected samples	The study did not involve field-collected samples.

Human research participants

Policy information about studies involving human research participants

Population characteristics	The human research participants varied within age and gender. They all were adult patients with IDH-mutated astrocytoma (WHO II° and III°), oligodendroglioma or glioblastoma of the University Hospital Heidelberg, University Hospital Mannheim, Helse Bergen or the Memorial Sloan Kettering Cancer Center. Patient samples were anonymised manually.
Recruitment	For human studies and xenograft models, samples were obtained from surgically resected adult glioblastoma and low-grade glioma patients from the department of neurosurgery at the University Hospital Heidelberg, University Hospital Mannheim, Helse Bergen, the department of neursurgery at Addenbrookes Hospital or the Memorial Sloan Kettering Cancer Center. All patients gave their informed consent for the scientific use of their resected parts.

Flow Cytometry

Plots

Confirm that:

☐ The axis labels state the marker and fluorochrome used (e.g. CD4-FITC).

☐ The axis scales are clearly visible. Include numbers along axes only for bottom left plot of group (a 'group' is an analysis of identical markers).

☐ All plots are contour plots with outliers or pseudocolor plots.

☐ A numerical value for number of cells or percentage (with statistics) is provided.

Methodology

Sample preparation	For FACS sorting, brain samples were prepared into cell suspension using the brain tumor dissociation kit (130-095-942, Miltenyi Biotec) and gentleMACSTM Dissociator (Miltenyi Biotec). Collected cell pellet was stained with Calcein Violet 450 AM (65-0854-39, Invitrogen) and TO-PRO®-3 Iodide (T3605, Invitrogen) to identify viable population. Tumor cells were separated based on their different fluorescent signals.
Instrument	FACS Canto II (BD Biosciences, V96300305)
Software	Data was collected with FACS Diva Software (version 9, BD Biosciences). Data was analysed with Flow Jo Version 10.5.x.
Cell population abundance	GFP-positive S24 glioma cells were >95 % positive post sort.
Gating strategy	Boundaries between positive and negative cells were defined by use of fluorescence minus one (FMO).

☐ Tick this box to confirm that a figure exemplifying the gating strategy is provided in the Supplementary Information.

Magnetic resonance imaging

Experimental design

Design type	n/a
Design specifications	n/a
Behavioral performance measures	n/a

Acquisition

Imaging type(s)	Structural
Field strength	1.5 Tesla, Siemens Avanto
Sequence & imaging parameters	T1-weighted sequence: in-plane-resolution: 0.977mm x 0.977mm, TR 1.9ms, TE 3.08ms, Acquisition matrix 256x246, Slice thickness: 1mm.
Area of acquisition	whole-brain-coverage

Diffusion MRI ☐ Used ☒ Not used

Preprocessing

Preprocessing software	n/a
Normalization	n/a
Normalization template	n/a
Noise and artifact removal	n/a
Volume censoring	n/a

Statistical modeling & inference

Model type and settings	n/a
Effect(s) tested	n/a

Specify type of analysis: ☐ Whole brain ☐ ROI-based ☐ Both

Statistic type for inference (See Eklund et al. 2016)	n/a
Correction	n/a

Models & analysis

n/a	Involved in the study
☐	☒ Functional and/or effective connectivity
☒	☐ Graph analysis
☒	☐ Multivariate modeling or predictive analysis

Functional and/or effective connectivity	Functional connectivity of the cells before and after channel-rhodopsin stimulation was investigated by determining the pairwise coactivity between single glioma cells. The similarity values between glioma cell traces were calculated. For each glioma cell, the calcium trace was vectorized in a n-dimensional space with n being the number of frames. The similarity index of each vector product was determined as the angle between the vectors in n-dimensional space.